

Accretion in the Early Kuiper Belt

II. Fragmentation

Scott J. Kenyon

Harvard-Smithsonian Center for Astrophysics

60 Garden Street, Cambridge, MA 02138

e-mail: skenyon@cfa.harvard.edu

and

Jane X. Luu

Leiden Observatory

PO Box 9513, 2300 RA Leiden, The Netherlands

e-mail: luu@strw.leidenuniv.nl

to appear in

The Astronomical Journal

July 1999

ABSTRACT

We describe new planetesimal accretion calculations in the Kuiper Belt that include fragmentation and velocity evolution. All models produce two power law cumulative size distributions, $N_C \propto r^{-2.5}$ for radii $\lesssim 0.3\text{--}3$ km and $N_C \propto r^{-3}$ for radii $\gtrsim 1\text{--}3$ km. The power law indices are nearly independent of the initial mass in the annulus, M_0 ; the initial eccentricity of the planetesimal swarm, e_0 ; and the initial size distribution of the planetesimal swarm. The transition between the two power laws moves to larger radii as e_0 increases. The maximum size of objects depends on their intrinsic tensile strength, S_0 ; Pluto formation requires $S_0 \gtrsim 300$ erg g $^{-1}$. The timescale to produce Pluto-sized objects, τ_P , is roughly proportional to M_0^{-1} and e_0 , and is less sensitive to other input parameters. Our models yield $\tau_P \approx 30\text{--}40$ Myr for planetesimals with $e_0 = 10^{-3}$ in a Minimum Mass Solar Nebula. The production of several ‘Plutos’ and $\sim 10^5$ 50 km radius Kuiper Belt objects leaves most of the initial mass in 0.1–10 km radius objects that can be collisionally depleted over the age of the solar system. These results resolve the puzzle of large Kuiper Belt objects in a small mass Kuiper Belt.

1. INTRODUCTION

Recent discoveries of slow-moving objects beyond the orbit of Neptune have radically changed our understanding of the outer solar system. These observations have revealed a large population of Kuiper Belt objects (KBOs) in orbits with semi-major axes of 39–45 AU (Jewitt & Luu 1993, 1995; Irwin *et al.* 1995; Williams *et al.* 1995; Jewitt *et al.* 1996; Luu *et al.* 1997; Gladman & Kavelaars 1997; Gladman *et al.* 1998). KBOs with reliable orbits have a cumulative size distribution that follows $N_C \propto r^{-q}$, with $q = 3 \pm 0.5$ (Jewitt *et al.* 1998; Luu & Jewitt 1998). The estimated population of $\sim 10^5$ KBOs with radii $r \gtrsim 50$ km indicates a total mass, $M_{KBO} \approx 0.1M_E$ ¹, for reasonable assumptions about the albedo and distance distribution.

The small mass in KBOs is a problem for current planet formation theories. In most theories, small planetesimals in the solar nebula grow by collisional accumulation (e.g., Safronov 1969; Greenberg *et al.* 1978, 1984; Wetherill & Stewart 1989, 1993; Spaute *et al.* 1991). This growth eventually produces one or more ‘cores’ that accumulate most, if not all, of the solid mass in an annular ‘feeding zone’ defined by balancing the gravity of the growing planetesimal with the gravity of the Sun and the rest of the disk. Large cores with masses of 1–10 M_E can also accrete gas from the feeding zone (Pollack 1984). Applied to the inner solar system, this model generally accounts for the masses of the terrestrial and gas giant planets (e.g., Pollack *et al.* 1996, Weidenschilling *et al.* 1997; but see Boss 1997). At 30–50 AU, however, the timescale to produce planet-sized, ~ 1000 km, objects exceeds the disk lifetime, $\lesssim 100$ Myr, unless the mass of the outer disk is $\sim 10^2$ – $10^3 M_{KBO}$ (e.g., Fernández & Ip 1981, 1984; Ip 1989; Stern 1995, 1996; Stern & Colwell 1997a). The presence of large KBOs in a small mass Kuiper Belt is thus a mystery.

In Kenyon & Luu (1998, hereafter KL98), we began to address this issue by considering planetesimal growth in a single annulus at 35 AU. We showed that calculations including accretion and velocity evolution naturally produce several “Plutos” with radii exceeding 1000 km and numerous 50 km radius KBOs on timescales of $\tau \sim 20$ – 200 Myr for a wide range of initial conditions in plausible solar nebulae. These timescales indicate that Pluto can form in the outer solar system in parallel with the condensation of the outermost large planets.

In this paper, we extend KL98 by adding fragmentation to our planetesimal evolution code. The code generally matches published calculations at 1 AU (Wetherill & Stewart 1993, hereafter WS93) and at 40 AU (Davis & Farinella 1997). Our numerical results

¹ $M_E = 6 \times 10^{27}$ g

demonstrate that fragmentation and velocity evolution damp runaway growth to provide a self-limiting mechanism for the formation of KBOs and Pluto in the Kuiper Belt. These calculations produce several Plutos and at least 10^5 50 km radius KBOs on timescales of 2–100 Myr in annuli with modest surface densities, 2.0–0.14 g cm⁻², of solid material at 35 AU. Our analysis sets a lower limit on the intrinsic strength of KBOs, ~ 300 erg g⁻¹, and indicates that the initial size distribution, the initial eccentricity of the planetesimal swarm, and the details of the fragmentation algorithm have little impact on the resulting size distribution of KBOs.

Our results appear to resolve the mystery of large KBOs in a small mass Kuiper Belt. Planetesimal evolution at 35–50 AU in a Minimum Mass Solar Nebula (Hayashi 1981) naturally produces large KBOs in numbers close to those currently observed. Most of the disk mass ends up in smaller objects, 0.1–10 km, that can be collisionally depleted over the age of the solar system. This depletion rate depends on the intrinsic strength and eccentricity distribution of KBOs (Stern 1996; Davis & Farinella 1997; Stern & Colwell 1997a, 1997b). Future observations can place better constraints on these physical parameters and provide additional tests of our interpretation of KBO formation.

We outline the fragmentation model and tests in Sec. 2, describe calculations for the Kuiper Belt in Sec. 3, and conclude with a discussion and summary in Sec. 4. The Appendix contains a complete description of the fragmentation algorithms and updates of the coagulation code from KL98.

2. The Model

As in KL98, we adopt Safronov’s (1969) particle-in-a-box method, where planetesimals are treated as a statistical ensemble of masses with a distribution of horizontal and vertical velocities about a Keplerian orbit. Our calculations begin with a differential mass distribution $n(m_i)$ in a single accumulation zone centered at a heliocentric distance a with an inner radius at $a - \Delta a/2$ and an outer radius at $a + \Delta a/2$. The horizontal and vertical velocity dispersions of these bodies are $h_i(t)$ and $v_i(t)$. We approximate the continuous distribution of particle masses with discrete batches having particle populations $n_i(t)$ and total masses $M_i(t)$ (WS93). The average mass of a batch, $m_i(t) = M_i(t)/n_i(t)$, changes with time as collisions add and remove bodies from the batch. This procedure naturally conserves mass and allows a coarser grid than calculations with fixed mass bins (Wetherill 1990; WS93).

To evolve the mass and velocity distributions in time, we solve the coagulation and

energy conservation equations for an ensemble of objects with masses ranging from $\sim 10^7$ g to $\sim 10^{26}$ g. The Appendix of KL98 describes our treatment of accretion and velocity evolution, and compares numerical results with analytic solutions for standard test cases. In this paper, we add fragmentation to the problem. We adopt a simple treatment of collision outcomes, following Greenberg *et al.* (1978; see also Davis *et al.* 1985, 1994; WS93):

1. Mergers – two bodies collide and merge into a single object with no debris;
2. Cratering – two bodies merge into a single object but produce debris with a mass much smaller than the mass of the merged object;
3. Rebounds – two bodies collide and produce some debris but do not merge into a single object; and
4. Disruption – two bodies collide and produce debris with a mass comparable to the mass of the two initial bodies.

We consider two algorithms for treating the cratering and disruption of planetesimals. Both the WS93 and the Davis *et al.* (1984) algorithms estimate the amount of debris $m_{f,ij}$ produced from impacts with velocities exceeding a threshold velocity V_f . In general, $m_{f,ij}$ scales with the impact energy. WS93 assume that the debris has the same relative velocity V_{ij} of the colliding bodies; Davis *et al.* (1984) assume that the debris receives a fixed fraction f_{KE} of the impact kinetic energy. In both cases, we adopt a coefficient of restitution c_R to allow for rebound collisions that produce debris but no single merged body. We follow Greenberg *et al.* (1978) and adopt separate values of c_R for collisions with (c_2) and without (c_1) cratering. The Appendix describes these algorithms in more detail.

To test our fragmentation procedures, we attempt to duplicate WS93’s calculations of planetary embryo formation at 1 AU. Their model begins with 8.33×10^8 planetesimals having radii of 8 km and a velocity dispersion of 4.7 m s^{-1} relative to a Keplerian orbit (Table 1; see also Table 1 of WS93). Table 2 summarizes our results using the WS93 initial conditions with mass spacing factors of $\delta \equiv m_{i+1}/m_i = 1.12, 1.25, 1.4,$ and 2.0 between successive mass batches. We adopt the analytic cross-sections of Spaute *et al.* (1991), which yield results identical to the numerical cross-sections of WS93 (KL98). Figure 1 shows our reproduction of WS93 for $\delta = 1.25$. This model produces twelve $3\text{--}7 \times 10^{25}$ g objects with velocity dispersions of $60\text{--}100 \text{ m s}^{-1}$ in 1.15×10^5 yr. In contrast, WS93 produce seven $1\text{--}3 \times 10^{26}$ g objects (see Figures 1–3 in WS93). Despite this factor of two difference in the total mass contained in the most massive bodies, our calculation has the same broad

“plateau” in the cumulative number distribution N_C at $\log m_i = 24\text{--}26$ and a similar power law dependence, $N_C \propto m_i^{-1}$, at $\log m_i = 21\text{--}23$. Our “fragmentation tail” at $\log m_i = 7\text{--}18$ has the standard power law dependence, $N_C \propto m_i^{-0.8}$ (Dohnanyi 1969), at large masses but flattens out more than the WS93 result at small masses.

The evolution of particle velocities in our calculations generally agrees with WS93 (Figure 2; see Figures 2–3 of WS93). All velocities increase monotonically with time due to viscous stirring. The velocities of large bodies grow very slowly, because dynamical friction transfers their kinetic energy to small bodies. The model maintains a nearly constant ratio of vertical to horizontal velocity, $v_i/h_i \approx 0.53$, for all but the most massive bodies, which have $v_i/h_i < 0.5$ (Figure 2, right panel). This result agrees with previous calculations (Barge & Pellat 1990, 1991; Hornung *et al.* 1985). At late times, our velocities for small bodies, $h_i \approx 200 \text{ m s}^{-1}$ at $m_i \sim 10^7 \text{ g}$, are roughly a factor of two larger than those of WS93. Velocities for large bodies, $h_i \approx 100 \text{ m s}^{-1}$ at $m_i \sim 10^{25} \text{ g}$, roughly equal those of WS93.

The higher velocities of our calculation lead to additional mass loss from gas drag and fragmentation. Gas drag removes material from the annulus; fragmentation produces bodies with masses less than the minimum mass, $\sim 10^7 \text{ g}$, of our numerical grid. We typically lose $\sim 25\%$ of the initial mass to cratering and catastrophic fragmentation and another 20% – 25% to gas drag. WS93 lost a comparable amount of mass to fragmentation but only $\sim 5\%$ to gas drag.

The agreement between our results and those of WS93 depends on the mass spacing factor δ . For $\tau \lesssim 30,000 \text{ yr}$, large δ models take longer to produce 1000–2000 km objects than small δ models. The ‘lag’ relative to our $\delta = 1.12$ model increases from 1% – 2% for $\delta = 1.25$ up to $\sim 10\%$ for $\delta = 2$ (see also Ohtsuki & Nakagawa 1988; Ohtsuki *et al.* 1990; Wetherill 1990; Kolvoord & Greenberg 1992; KL98). The poor resolution of $\delta \geq 1.4$ models delays the production of massive bodies that ‘runaway’ from the rest of the mass distribution. In WS93, most runaway bodies are also ‘isolated’ bodies that do not interact with one another but do interact with the rest of the mass distribution (see WS93 and the Appendix). Delays in the production of isolated, runaway bodies lead to 10% – 20% increases in the velocity dispersion of all bodies. Larger velocities reduce gravitational focusing factors and slow the growth of the largest bodies. The mass of the largest object thus increases from $7\text{--}8 \times 10^{25} \text{ g}$ for $\delta = 1.25\text{--}1.4$ to $9.5 \times 10^{25} \text{ g}$ for $\delta = 1.12$. This trend suggests that calculations with $\delta = 1.01\text{--}1.10$, as in WS93, would improve the agreement between our results and those of WS93.

The coagulation results also depend on the treatment of low velocity collisions. Our standard expressions for long-range gravitational interactions fail when the velocity

dispersion is close to the Hill velocity, v_H (Ida 1990; Barge & Pellat 1991). We use Ida’s (1990) n -body calculations and adopt his simple expressions to derive the velocity evolution for collisions in the low velocity limit, $V_{ij} < V_{lv}v_H$, where $V_{lv} = 2\text{--}5$ is a constant (see the Appendix). This change slows down the velocity evolution, because it introduces a lower limit to the timescales for dynamical friction and the inclination component of viscous stirring (Ida 1990). We adopt $V_{lv} = 2$, following WS93, for 1 AU calculations. Unlike WS93, however, the small bodies in our calculation do not quite reach the low velocity limit and increase in velocity throughout the evolution. A modest increase in our low velocity limit, $V_{lv} = 3.5$, leads to better agreement between the velocity behavior of our models and that of WS93.

To test our procedures further, we repeat the 1 AU calculations using the Davis *et al.* (1984) fragmentation algorithm. Table 3 lists our results for $f_{KE} = 0.1$ and $\delta = 1.25, 1.4$, and 2.0. These calculations yield solutions similar to our WS93 models. Calculations with smaller δ produce larger bodies at earlier times than models with large δ (Table 3). The mass of the largest object increases from $m_i \approx 7 \times 10^{25}$ g for $\delta = 2.0$ to $m_i \approx 1.2 \times 10^{26}$ g for $\delta = 1.4$ to $m_i \approx 1.8 \times 10^{26}$ g for $\delta = 1.25$. The velocity dispersions of the small bodies are a factor of 2–3 larger at $\tau \lesssim 30,000$ yr because they receive a larger fraction of the fragmentation energy than in the WS93 algorithm. This trend reverses for $\tau \gtrsim 50,000$ yr, because the Davis *et al.* algorithm produces more debris for collisions between large objects than the WS93 algorithm. These large objects have small velocity dispersions, so the velocity dispersions of the small bodies increase more slowly than in the WS93 model. The mass lost from fragmentation, $\sim 5\%$ of the initial mass, and gas drag, $\sim 20\%$ of the initial mass, is also smaller.

We conclude that our coagulation code with fragmentation and velocity evolution reproduces ‘standard’ calculations. The results in Tables 2–3 generally agree with published results, despite some differences in the evolution of the velocity dispersion and the radius of the largest object. These discrepancies probably result from subtle differences in the implementation of the algorithms. None seem significant, because the major results do not depend on the input parameters (see also WS93): all calculations produce several objects with $m_i \sim 10^{26}$ g that contain most of the remaining mass in the annulus.

3. Kuiper Belt Calculations

3.1. Starting Conditions

As in KL98, we rely on observations of other stellar systems and solar nebula models to choose appropriate initial conditions for our Kuiper Belt calculations. Recent observations indicate lifetimes of $\sim 5\text{--}10$ Myr for typical gaseous disks surrounding nearby pre-main-sequence stars and for the solar nebula (Sargent & Beckwith 1993; Russell *et al.* 1996; Hartmann *et al.* 1998). In our solar system, Neptune formation places another constraint on the KBO growth time, because Neptune excites KBOs through gravitational perturbations. Recent calculations suggest Neptune can form in 5–100 Myr (Ip 1989; Lissauer *et al.* 1996; Pollack *et al.* 1996). Once formed, Neptune inhibits KBO formation at 30–40 AU by increasing particle random velocities on timescales of 20–100 Myr (Holman & Wisdom 1993; Duncan *et al.* 1995; Morbidelli & Valsecchi 1997). We thus adopt 100 Myr as an upper limit to the KBO formation timescale at 30–40 AU.

Our starting conditions for KBO calculations are similar to KL98. We consider an annulus centered at 35 AU with a width of 6 AU. This annulus can accommodate at least 10–100 isolated bodies with $m_i \gtrsim 10^{24}$ g for $e \leq 0.01$. Instead of the single starting radius used in KL98, the present calculations begin with N_0 bodies in a size distribution with radii, $r_i = 1\text{--}80$ m. This initial population has a power law cumulative size distribution, $N_C \propto r_i^{-q_0}$. We usually adopt $q_0 = 3$; the final size distribution appears to depend very little on q_0 , as discussed below. The planetesimals have a small initial eccentricity (Malhotra 1995) that is independent of size and an equilibrium ratio of inclination to eccentricity, $\beta_0 = \langle i_0 \rangle / \langle e_0 \rangle = 0.6$ (Barge & Pellat 1990). The mass density of each body is 1.5 g cm^{-3} . To set the initial mass of the annulus, M_0 , we extend the Minimum Mass Solar Nebula to the Kuiper Belt and integrate the surface density distribution for solid particles, $\Sigma = \Sigma_0 (a/a_0)^{-3/2}$, across the 6 AU annulus. The dust mass is then $M_{min} \approx 0.25 \Sigma_0 M_E$ at 32–38 AU for $a_0 = 1$ AU. Most Minimum Mass Solar Nebula models have $\Sigma_0 = 30\text{--}60 \text{ g cm}^{-2}$ (Weidenschilling 1977; Hayashi 1981; Bailey 1994), which sets $M_{min} \approx 7\text{--}15 M_E$. We consider models with $M_0 = 1\text{--}100 M_E$ to allow for additional uncertainty in Σ_0 . Table 1 compares input parameters for Kuiper Belt models with initial conditions at 1 AU (see also WS93).

Our success criteria are based on available observations of KBOs. The present day Kuiper Belt contains (a) at least one object (Pluto) with radius $\gtrsim 1000$ km and (b) $\sim 70,000$ objects with radii exceeding 50 km (Jewitt & Luu 1995; Jewitt *et al.* 1996, 1998). A successful KBO calculation must satisfy both observed properties in $\lesssim 100$ Myr. We quantify these criteria by defining r_{max} as the radius of the largest object and r_5 as the

radius where the cumulative number of objects is $N_C \geq 10^5$: a successful simulation has $r_{max} \gtrsim 1000$ km and $r_5 \gtrsim 50$ km at $\tau \lesssim 100$ Myr. To provide another characteristic of these models, we define $r_{95\%}$ such that 95% of the mass is contained in objects with $r_i < r_{95\%}$. In models with a long runaway growth phase, the largest objects contain most of the mass and $r_{95\%} \approx r_5$. Models with a limited runaway growth phase leave most of the mass in small objects, so $r_{95\%} \ll r_5$. We end calculations with velocity evolution when r_{max} exceeds ~ 1000 km. To evaluate the dependence of runaway growth on fragmentation, we extend calculations without velocity evolution to 5000 Myr or to when r_{max} exceeds ~ 2000 – 3000 km.

3.2. Models Without Velocity Evolution

To isolate how fragmentation changes the growth of KBOs, we begin with constant velocity calculations of accretion. The initial size distribution has $q_0 = 3$, $\delta = 1.4$, and a maximum initial radius of $r_0 = 80$ m. The initial velocities of $h_i = 4$ m s $^{-1}$ and $v_i = 2.1$ m s $^{-1}$ correspond to an equilibrium model with $e_0 = 10^{-3}$ (Hornung *et al.* 1985). We use the Davis *et al.* (1985) fragmentation algorithm and assume that the collision fragments receive a kinetic energy per unit mass equal to one-half of the square of the relative velocity of the colliding bodies, V_{ij} . The bodies are strong, with a tensile strength $S_0 = 2 \times 10^6$ erg g $^{-1}$. Tables 1 and 4 summarize the initial conditions and results for models with $M_0 = 1$ – 100 M_E , $e_0 = 10^{-3}$, and the coefficients of restitution, $(c_1, c_2) = (10^{-5}, 10^{-5})$ and $(10^{-2}, 10^{-3})$.

Figure 3 shows how N_C evolves with time for $M_0 = 10$ M_E , $e_0 = 10^{-3}$, and $(c_1, c_2) = (10^{-5}, 10^{-5})$. The low coefficients of restitution eliminate rebound collisions. Roughly half of the most massive objects experiences at least one collision by $\tau \approx 16$ Myr, when the 18 largest bodies have $r_i \approx 1$ km. These bodies reach $r_i \sim 10$ km at $\tau \approx 135$ Myr and grow to 100 km sizes at 255 Myr. The growth rate then increases considerably due to gravitational focusing. Runaway growth ensues. The largest planetesimals reach $r_{max} \approx 200$ km at $\tau \approx 265$ Myr; r_{max} exceeds 1000 km only 11 Myr later. At $\tau \approx 280$ Myr, a single runaway body with $r_{max} \approx 2000$ km begins to sweep up lower mass planetesimals and contains nearly all of the mass in the annulus a few Myr later.

The cumulative size distribution of small objects with $r_i \lesssim 100$ m slowly approaches a power law with $q = 2.25$ throughout the evolution. The distribution is shallow, $q < 2$, for $\tau \lesssim 20$ Myr as growth produces many 50–500 m objects. The distribution steepens as the largest bodies grow past 1 km and settles at $q = 2.25$ for $\tau \gtrsim 150$ Myr. This distribution is steeper than the theoretical limit of $q = 2.5$ (Dohnanyi 1969; Williams & Wetherill 1994), because growth and fragmentation never reach equilibrium.

Calculations with rebound collisions yield similar results. With larger coefficients of restitution, $(c_1, c_2) = (10^{-2}, 10^{-3})$, rebound collisions occur for $r_i \lesssim 5$ m. These collisions produce fragments but no mergers into larger bodies. As a result, the size distribution is initially very steep for $r_i \lesssim 5$ m and very shallow for $r_i \gtrsim 5$ m (Figure 4). As the largest objects grow from 1 km to 10 km at $\tau = 16$ –135 Myr, bodies with $r_i \lesssim 5$ m are swept up by the large bodies and replaced by collision fragments. This process smooths out the size distribution at $r_i \sim 1$ –20 m, although the slope still changes at $r_i \sim 5$ m.

The evolution of the largest bodies is unaffected by rebounds. These objects reach sizes of 100 km only slightly later than models without rebounds, 258 Myr *vs* 255 Myr, and then begin to runaway from lower mass planetesimals. Several objects reach radii of 1000 km in another ~ 20 Myr and then begin to consume all of the material left in the annulus.

Fragmentation is not important in any of these low eccentricity calculations. Catastrophic fragmentation produces no mass loss. because the velocities remain artificially low. These models lose only 1%–3% of their initial mass due to cratering. The timescale to grow into a 1000 km object is nearly identical to models without fragmentation (see KL98): Pluto forms in $\tau_P \approx 276$ –280 Myr $(M_0/10 M_E)^{-1}$ for $r_0 = 80$ m. Calculations with larger r_0 should have smaller growth times (see KL98).

3.3. Models With Limited Velocity Evolution

To understand how fragmentation changes the velocity dispersions of colliding planetesimals, we consider calculations with ‘limited’ velocity evolution. As in Davis *et al.* (1985, 1994), we assume that collision fragments receive a fixed fraction f_{KE} of the center-of-mass impact energy, but consider no other changes to the kinetic energy of the bodies. For most collisions, this assumption produces fragments with velocities larger than the relative collision velocity V_{ij} . To conserve kinetic energy, the merged bodies have a lower velocity dispersion after the collision. This redistribution of velocity mimics dynamical friction and should lead to more rapid growth than models with no velocity evolution. Table 5 summarizes results for $e_0 = 10^{-3}$, $S_0 = 2 \times 10^6$ erg g $^{-1}$, and coefficients of restitution, $(c_1, c_2) = (10^{-2}, 10^{-3})$, for our standard mass distribution with $q_0 = 3$, $\delta = 1.4$, and $r_0 = 80$ m.

Figure 5 shows how N_C evolves with time for $M_0 = 10 M_E$. During the first 10–20 Myr, the size distribution has two power laws, $q \approx 4$ for $r_i \lesssim 5$ m and $q \approx 1.25$ for $r_i \gtrsim 5$ m. This break in the slope is due to rebounds, which prevent growth of the smallest objects. As the largest objects grow to sizes of 1–10 km, collision debris adds to the population of

5 m objects. The slope of the size distribution is then $q \approx 2.5$ for $r_i \lesssim 100$ m. For large objects, q approaches 2.5 once r_{max} exceeds 100 km. Once $r_{max} \gtrsim 1000$ km, the complete number distribution follows a power law with $q = 2.5$, except for a small kink at $r_i \approx 1$ km whose amplitude decreases with time.

Limited velocity evolution eventually produces larger objects on shorter timescales than models without velocity evolution. In the first 20–40 Myr, collisions between the largest bodies, $r_i \approx 100$ –500 m, add material with high velocity dispersion to batches with $r_i \sim 1$ –10 m. The horizontal velocity dispersions of these low mass objects increase from 4 m s^{-1} to 10 – 30 m s^{-1} in 17 Myr and reach a roughly constant value of $\sim 20 \text{ m s}^{-1}$ after 200 Myr (Figure 6). This large velocity dispersion initially slows down the growth of the largest objects relative to models with no velocity evolution. It takes this model ~ 1 Myr longer to produce objects with $r_i \sim 1$ km, but these objects then have velocities $\sim 1 \text{ m s}^{-1}$ smaller than the initial velocity of the planetesimal swarm (see Figure 6). This smaller velocity dispersion enhances the growth of the largest objects once gravitational focusing becomes important. The model produces 10 km objects in 120 Myr and 100 km objects in 202 Myr. This rapid evolution leads to runaway growth and the production of a few 1000+ km objects after another 15 Myr.

Figure 7 compares r_{max} in models with no velocity evolution (thin solid lines) and models with limited velocity evolution (thick solid lines). The annuli have initial masses $M_0 = 1, 10,$ and $100 M_E$. These models are nearly indistinguishable for $r_{max} \lesssim 10$ km. The limited velocity evolution models then produce larger objects on shorter timescales. These models do not have a mass-dependent velocity evolution such as viscous stirring or dynamical friction, so the timescale to produce 1000 km objects is still inversely proportional to the mass in the annulus, $\tau_P = 216 \text{ Myr} (M_0/10 M_E)^{-1}$ for $e_0 = 10^{-3}$.

Other than the accelerated growth rate at late times, there is little difference between models with limited velocity evolution and models with no velocity evolution (see Tables 4–5). Both sets produce comparable numbers of large KBOs, $r_i \gtrsim 100$ km, that contain most of the mass in the annulus when the first Pluto forms. These models also lose $\sim 1\%$ – 3% of their initial mass due to cratering. The mass loss depends solely on the total kinetic energy of all the bodies, which is a constant in these models. Catastrophic fragmentation still produces no mass loss, because we assume relatively strong objects with $S_0 = 2 \times 10^6 \text{ erg g}^{-1}$. We describe models with weaker bodies in the next section.

3.4. Models with Velocity Evolution

We now consider a complete coagulation calculation with fragmentation and velocity evolution. In addition to velocity redistribution from fragmentation, these models include (i) gas drag, (ii) dynamical friction and viscous stirring from long-range (elastic) collisions, and (iii) dynamical friction and viscous stirring from short-range (inelastic) collisions (see the Appendix of KL98). To approximate the disappearance of the solar nebula on reasonable timescales, we assume that the gas density decays exponentially with time, $\rho_g(t) = \rho_{g,0} e^{-t/\tau_g}$ where $\rho_{g,0} = 1.18 \times 10^{-9} (a/1AU)^{-21/8} (M_0/4M_E)$ g cm⁻³ (WS93 and references therein). The influence of gas drag on the planetesimals thus decreases with an e -folding time of τ_g , which we set at $\tau_g = 10$ Myr (Hartmann *et al.* 1998). We adopt $\delta = 1.4$, $q_0 = 3$, and $r_0 = 80$ m. The initial velocities are $h_i = 4.0 (e_0/10^{-3})$ m s⁻¹ and $v_i = 2.1 (e_0/10^{-3})$ m s⁻¹. Tables 6–7 summarize the initial conditions and results for models with $M_0 = 1\text{--}100 M_E$ and $e_0 = 10^{-4}$ to 10^{-2} .

3.4.1. A Standard Model with $e_0 = 10^{-3}$ and $S_0 = 2 \times 10^6$ erg g⁻¹

Figure 8 shows how N_C and h_i evolve for $M_0 = 10 M_E$, $e_0 = 10^{-3}$, and $S_0 = 2 \times 10^6$ erg g⁻¹. Inelastic collisions act rapidly to circularize the orbits of objects with $r_i \gtrsim 5$ m, which decrease in velocity from $h_i = 4$ m s⁻¹ to $h_i = 1\text{--}2$ m s⁻¹ in 5 Myr. Larger bodies have less frequent collisions; their orbits circularize on longer timescales. Small bodies with $r_i \lesssim 5$ m collide frequently, but rebounds prevent these bodies from circularizing their orbits. Instead, collision fragments increase the velocity dispersion of the lowest mass bodies. These processes produce an inverted velocity distribution, where bodies with $r_i \approx 5$ m have smaller velocities than objects with $r_i \lesssim 5$ m and $r_i \gtrsim 10$ m.

The steady damping of particle velocities enhances growth of the larger bodies relative to calculations with limited velocity evolution. The largest objects grow slowly for 8.5 Myr, when there are ~ 500 objects with $r_i = 1$ km. The size distribution then has three main features: (i) a pronounced fragmentation tail with a modest velocity dispersion, $h_i \approx 1\text{--}3$ m s⁻¹; (ii) a transition region with pronounced kink in the size distribution; and (iii) a group of rapidly growing bodies with low velocities, $h_i = 0.02$ m s⁻¹ (Figure 8; left panel). These features remain prominent as r_{max} increases from 1 km to 100 km in only 3.5 Myr.

During runaway growth, dynamical friction and viscous stirring begin to increase particle velocities (Figure 8; right panel). This phase ends when r_{max} reaches ~ 300 km at 15 Myr. The velocity dispersions of the small to intermediate mass bodies are then large enough, ~ 10 m s⁻¹, to reduce gravitational focusing factors considerably. The largest

objects enter a steady growth phase, where their radii grow slowly with time. There are 2 Charon-sized objects with $r_i \gtrsim 500$ km at 19 Myr; 50 “Charons” at 25 Myr, and ~ 150 Charons at 36.5 Myr when the first “Pluto” appears. The size distribution then closely follows a power law with $q = 2.5$ for $r_i \lesssim 30$ m and a steeper power law with $q = 3$ for $r_i = 1\text{--}1000$ km. The modest velocity dispersion of the largest objects, $h_i \approx 0.5$ m s $^{-1}$, maintains steady growth for another 60 Myr: 4 objects have $r_i = 1450$ km at 50 Myr; 8 objects have $r_i = 2000$ km at 100 Myr.

Figure 9 illustrates how the largest objects grow as a function of M_0 . All models begin with slow growth, where inelastic collisions reduce the velocity dispersions of the intermediate mass objects. Slow growth lasts longer as M_0 decreases, because the growth rate depends on the collision rate. Viscous stirring prolongs the slow growth phase of small M_0 models by counteracting collisional damping earlier in the evolution. Slow growth thus produces more 1–2 km objects in models with smaller M_0 . Runaway growth eventually turns 1 km bodies into 100 km objects. This phase ends when bodies with $r_i \lesssim 1$ km have velocity dispersions exceeding 10–20 m s $^{-1}$. The large gravitational focusing factors that began runaway growth are then smaller by several orders of magnitude. The growth then returns to a steady phase where the largest bodies gradually approach radii of 1000 km.

In these models, cratering also acts to damp runaway growth. As noted in Sect. 3.3, collision debris increases the velocities of the smallest objects. Viscous stirring and dynamical friction enhance this evolution as the largest objects grow beyond 1 km. The velocity dispersions of small objects increase from ~ 20 m s $^{-1}$ at the end of runaway growth to ~ 100 m s $^{-1}$ at 100 Myr. The largest objects then have $r_i \approx 2000$ km. Collision debris produces $\sim 30\%$ of this increase; dynamical friction and viscous stirring are responsible for the rest.

Although all models with $e_0 = 10^{-3}$ make at least one Pluto, only annuli with $M_0 \sim 10 M_E$ meet both success criteria. In each calculation, r_5 steadily increases with time during the slow growth phase (Figure 10). The number of 50 km radius KBOs increases dramatically during runaway growth, when gravitational focusing factors are large. At the end of runaway growth, r_5 begins to decrease with time as the largest bodies try to separate themselves from the rest of the mass distribution. This evolution is modest and short-lived, because the runaway growth phase ends quickly. The number of 50 km radius KBOs then approaches a roughly constant value which grows with increasing M_0 . Based on Figure 10, annuli with $M_0 \lesssim 3 M_E$ produce too few 50 km radius KBOs compared with our success criterion; annuli with $M_0 \gtrsim 30 M_E$ probably produce too many. Annuli with $3 M_E \lesssim M_0 \lesssim 30 M_E$ can produce 1 or more Plutos and roughly 10^5 KBOs in $\lesssim 100$ Myr.

This ‘standard model’ has several important input parameters, including the initial

eccentricity, the initial size distribution, and the intrinsic strength of the bodies. To understand how the evolution depends on these parameters, we now consider variations on the standard model. We begin with a discussion of e_0 and then describe models with different input strengths and size distributions.

3.4.2. Models with $e_0 = 10^{-4}$ and 10^{-2} for $S_0 = 2 \times 10^6 \text{ erg g}^{-1}$

The velocity dispersion of the planetesimal swarm affects growth primarily through gravitational focusing. Large bodies grow faster when velocity dispersions are small and gravitational focusing factors are large. Despite small e_0 , all of our calculations begin in the “high velocity regime,” where gravitational focusing factors are near unity. Collisional damping and dynamical friction reduce velocity dispersions to the low velocity regime where growth is rapid. Planetesimals with small e_0 can reach this regime first, so we expect that smaller e_0 leads to more rapid growth.

Calculations with $e_0 = 10^{-4}$ and 10^{-2} confirm these general considerations. In models with $e_0 = 10^{-2}$, the larger initial velocities reduce collisional damping compared to models with $e_0 = 10^{-3}$. Gravitational focusing factors thus increase slowly. Additional cratering debris also counteracts collisional damping and combines with dynamical friction and viscous stirring to keep velocity dispersions large. As a result, models with $e_0 = 10^{-2}$ experience a prolonged linear growth phase. This phase is ~ 10 times longer than for $e_0 = 10^{-3}$ models. Slow growth ends when the largest objects reach the sizes needed to produce modest gravitational focusing factors. A short runaway growth phase eventually produces several Plutos. The final size distribution has a larger fraction of mass in more massive objects, as indicated by a large value for $r_{95\%}$, but has roughly comparable numbers of 50 km radius KBOs (Table 6). These models also lose more mass to dust, $\sim 50\%$, compared to the 1%–3% lost in models with $e_0 = 10^{-3}$.

Growth is rapid in models with $e_0 = 10^{-4}$, because collisional damping quickly reduces the velocity dispersion. This change does not have a dramatic effect on the growth of KBOs, because damping quickly reduces particle velocities to the low velocity limit. The damping time is then independent of velocity. Viscous stirring is also less effective. In our calculations, the growth times for $e_0 = 10^{-4}$ models are a factor of ~ 2 –10 smaller than $e = 10^{-3}$ models (Table 6). Models with $e_0 \lesssim$ a few $\times 10^{-5}$ probably have similar growth times, but we have not investigated this possibility in detail.

Figure 11 compares the size distribution near the end of our calculations for three different values of e_0 . All models produce two power law size distributions, with $q = 2.5$ for

small objects and $q = 3$ for large objects. These power laws are connected by a transition region which moves to larger radii with increasing e_0 . The fragmentation population thus extends to larger radii with *larger* e_0 . In contrast, the merger population (the steep power law at larger radii) extends to smaller radii with *smaller* e_0 . This feature of the calculations can be tested directly with observations (Kenyon & Luu 1999)

3.4.3. Models with Weaker Bodies

The intrinsic strength S_0 of a planetesimal changes the growth rate by setting the impact energy Q_d needed to disrupt colliding bodies. In our disruption model, Q_d depends on the sum of S_0 and the gravitational binding energy of a colliding pair of planetesimals, $4\pi G\rho_0 R_c^2/15$ (eq. [A11] and [A13]). The gravitational term is small compared to S_0 when the combined radius of the merged object is $R_c \lesssim 0.03S_0^{1/2}$ km. The maximum radius of our initial size distribution, $r_0 = 80$ m, falls below this limit for $S_0 \lesssim 25$ erg g⁻¹. For collisions between equal mass bodies, we can then derive a simple expression relating the minimum strength necessary for growth and the velocity dispersion,

$$S_{0,min} \approx 6 \times 10^4 \text{ erg g}^{-1} \left(\frac{V_{ij}}{100 \text{ m s}^{-1}} \right)^2 \quad (1)$$

At the start of our calculations, this result yields

$$S_{0,min} \approx 300 \text{ erg g}^{-1} \left(\frac{e_0}{10^{-3}} \right)^2. \quad (2)$$

Bodies with $e_0 \lesssim 0.1$ initially grow for the standard case with $S_0 = 2 \times 10^6$ erg g⁻¹. As these objects grow to 1 km sizes, viscous stirring and dynamical friction increase the velocities of small objects. Once the velocities reach the threshold set by Equation (1), catastrophic disruption produces debris that is lost from the calculation. This process should limit the growth of the largest objects by reducing the reservoir of small bodies available for accretion. We thus expect the maximum size of KBOs to depend on S_0 .

To test these ideas in detail, we consider models with various S_0 . Calculations with $S_0 = 10$ to 2×10^6 erg g⁻¹ for $e_0 = 10^{-4}$ and $S_0 = 10^4$ to 2×10^6 erg g⁻¹ for $e_0 = 10^{-3}$ allow velocity evolution to increase particle velocities up to the disruption threshold. Models with $S_0 \lesssim 2 \times 10^6$ erg g⁻¹ and $e_0 \gtrsim 10^{-3}$ lose too much mass in the early stages to be of much practical value. Models with $S_0 \gtrsim 2 \times 10^6$ erg g⁻¹ are identical to models with $S_0 = 2 \times 10^6$ erg g⁻¹.

Table 7 summarizes our results at 50 Myr and 100 Myr for $M_0 = 10 M_E$ and several different values of δ . For both values of e_0 , stronger objects can grow to larger sizes at 100 Myr (see Figure 12). In each model, accretion and collisional damping lead to a short runaway growth phase that produces 100+ km objects with low velocities ($h_i \lesssim 0.1 \text{ m s}^{-1}$), but leaves most of the initial mass in 0.1–1 km objects with much larger velocities ($h_i \sim 3\text{--}10 \text{ m s}^{-1}$). Dynamical friction and viscous stirring then increase the velocities of these small objects to the disruption threshold. The timescale to reach this threshold increases with S_0 ; r_{max} also increases with S_0 as indicated in Table 7 and Figure 12. When all small bodies have been disrupted, the maximum radius is nearly independent of δ :

$$\log r_{max} \approx 2.45 + 0.22 \log S_0 \quad (3)$$

for $10 \text{ erg g}^{-1} \leq S_0 \leq 10^4 \text{ erg g}^{-1}$ and $e_0 = 10^{-4}$ and 10^{-3} . We did not run models with larger S_0 to the disruption threshold. Future calculations will allow us to see whether r_{max} reaches a threshold value at large S_0 or continues to increase as indicated by Equation (3).

Although r_{max} depends on S_0 , both r_5 and the slope of the final size distribution at large radius are independent of S_0 . The radius limit for 10^5 KBOs has a small range, $r_5 \approx 45\text{--}60 \text{ km}$, for any combination of δ and S_0 (Table 7). Figure 13 shows the evolution of the size distribution for $S_0 = 10 \text{ erg g}^{-1}$. As in Figure 8 and Figure 11, accretion produces a fragmentation tail with $q = 2.5$ at small radii and a steeper power law with $q = 3$ at large radii. The $q = 3$ power law persists throughout the catastrophic disruption phase; the fragmentation tail evolves into a very steep power law with $q = 4$. This behavior of the fragmentation tail occurs because larger objects initially experience more disruptive collisions than do smaller objects. Catastrophic disruption adds high velocity fragments from larger objects to the smaller mass bins; kinetic energy from this debris and viscous stirring gradually push smaller and smaller objects over the disruption threshold. Eventually, the smallest objects in our grid, $r_i \approx 1 \text{ m}$, reach the disruption threshold and are slowly removed from the calculation.

3.4.4. Models with Different Size Distributions

The initial size distribution is one of the most uncertain input parameters of our coagulation models. The growth of 1–10 m or larger bodies from interstellar dust grains is poorly understood. Predicted sizes for conditions in the outer solar system range from $\lesssim 1 \text{ m}$ up to several hundred km depending on details of both microscopic and macroscopic physics (e.g., Goldreich & Ward 1973; Tremaine 1990; Cuzzi *et al.* 1993a,

1993b; Bailey 1994; Weidenschilling 1997; Boss 1997; Wurm & Blum 1998). To test the sensitivity of our results to the initial conditions, we consider models with (a) $q_0 = 4.5$, (b) $q_0 = 1.5$, and (c) $N_C = \text{Const } \delta(r - r_0)$. These models produce final size distributions that are indistinguishable from our standard model with $q_0 = 3$. Both r_{max} and r_5 are also independent of the initial size distribution. The time to runaway growth and the timescale to produce one Pluto increase with the amount of material initially in the smallest objects, because collisional damping is more effective when there is a large reservoir of small objects. We derive $\tau_P = 30$ Myr for $q_0 = 4.5$, $\tau_P = 37$ Myr for $q_0 = 3$, $\tau_P = 42$ Myr for $q_0 = 1.5$, and $\tau_P = 49$ Myr for $N_C = \text{Const } \delta(r - 80 \text{ m})$.

To test the importance of the mass spacing factor, we recomputed these models for $\delta = 1.25$. Our results for (a), (b), and (c) in the preceding paragraph are indistinguishable from results with $\delta = 1.4$, except that the timescale to produce Pluto decreases by $\sim 5\%$. The model with $\delta = 1.25$ and our standard initial size distribution, $q_0 = 3$, produced a single large body that ran away from the rest of the large bodies. The final radius of this single object is $\sim 50\%$ larger than r_{max} for other calculations with $M_0 = 10M_E$. Several tests indicate that forming a single large body is a stochastic process sensitive to δ : small δ models produce such an object more often than large δ models. We plan to investigate this possibility further in future studies.

3.4.5. Other Input Parameters

To conclude this section, we briefly comment on the sensitivity of our calculations to other input parameters listed in Table 1. The results described above are insensitive to factor of two variations in the particle mass density ρ_0 , the relative gas velocity η , the minimum velocity for cratering V_f , and the crushing energy Q_c . We suspect that factor of ten variations in η , V_f , and Q_c will also have no impact on the results. Larger variations in ρ_0 would probably change the variation of r_{max} with S_0 in Table 7, but we have not investigated this possibility. Increasing the fraction of kinetic energy imparted to fragmentation debris f_{KE} decreases the time needed to produce 100+ km objects². The growth time decreases by $\sim 10\%$ for $f_{KE} = 0.1$ and $\sim 20\%$ for $f_{KE} = 0.2$. Variations in the input f_{KE} do not change the final size distribution or the number of KBOs as a function of M_0 . This parameter thus has less impact on the results than either e_0 or S_0 .

²In contrast, use of the WS93 fragmentation algorithm increases the time needed to produce 100+ km objects, although this increase is $\lesssim 10\%$ – 20%

3.5. Limitations of the Models

We summarized the major uncertainties of our planetesimal calculations in KL98 and will repeat important points for the current models here. Our choice of a single accumulation zone does not allow us to follow the evolution in semimajor axis of a planetesimal swarm (Spaute *et al.* 1991; Weidenschilling *et al.* 1997). Although multi-zone calculations are important for understanding migration and other long-term aspects of planetesimal evolution, single-annulus models are a reasonable first approximation for the early evolution of KBOs. The growth of large nearby bodies, such as those that will merge to form Neptune, should modify the velocity evolution of KBOs once these bodies reach sizes much larger than 1000 km (see Morbidelli & Valsecchi 1997). For most solar nebulae, these long-distance interactions should remain small until Pluto forms beyond 30 AU (KL98; see also Lazzaro *et al.* 1994; Roques *et al.* 1994; Morbidelli & Valsecchi 1997; Ward & Hahn 1998). Calculations now underway will test this assertion in more detail.

Our relatively coarse mass grid probably overestimates the timescale to produce KBOs and Pluto by $\sim 5\%$ – 10% (KL98). The delay in runaway growth relative to a $\delta = 1.25$ model is 3% – 5% for $\delta = 1.4$ and 5% – 10% for $\delta = 2.0$. Although these delays are small compared to the overall uncertainties in our algorithms, calculations with $\delta \gtrsim 2$ rarely produce one or more isolated bodies that grow much faster than smaller bodies. The better mass resolution of $\delta \lesssim 1.4$ calculations allows more mass batches to satisfy the isolation condition, defined in the Appendix, which leads to more accurate calculations of the cumulative mass distribution and the velocity evolution of the lowest mass objects.

The lack of a rigorous treatment of gas dynamics probably has little impact on our results. Gas drag removes $\lesssim 1\%$ of the initial mass from these models. Gas accretion by large bodies is also insignificant. The minimum radius needed to capture gas from the disk is $r_i \sim 1000$ – 2000 km for typical temperatures of 50–100 K at 30–50 AU (Beckwith *et al.* 1990; Osterloh & Beckwith 1994). Our models reach this limit on timescales exceeding the lifetime of the gaseous disk, so we expect little gas accretion by Kuiper Belt bodies.

Our calculations probably overestimate the amount of mass lost to dust. At both 1 AU and 35 AU, losses from catastrophic fragmentation, cratering, and gas drag grow with increasing δ . In large δ models, small delays in the formation of runaway bodies allow dynamical friction and viscous stirring extra time to increase the velocity dispersions, and hence mass loss, of the smallest objects. These effects are probably small, $\sim 10\%$ – 20% , for most of our calculations.

Our choice of the initial size distribution has little impact on our results. Models with $q_0 = 1.5$ and $q_0 = 4.5$ produce final size distributions very similar to those for calculations

with $q_0 = 3$. The timescale to produce 1000 km objects lengthens as q_0 decreases. The ‘equilibrium’ size distribution with $q = 3$ is similar to the observed size distribution of interstellar dust grains, $q \approx 2\text{--}3$ (e.g, Kim *et al.* 1994; Li & Greenberg 1997 and references therein). Similar size distributions are derived from calculations of the growth of very small particles using measured sticking efficiencies (e.g., Wurm & Blum 1998).

Aside from the timescale to produce 1000 km objects and the amount of mass lost to gas drag and fragmentation, the initial eccentricity distribution probably also has little impact on our conclusions. The number of 50 km radius KBOs is not sensitive to e_0 ; $r_{95\%}$ increases with e_0 only for $e_0 \gtrsim 10^{-2}$ (Table 6). The slope of the final size distribution is also insensitive to e_0 .

We suspect that initial eccentricities outside the range considered here are unrealistic. Viscous stirring and gas drag appear to set a lower limit on the eccentricity of small objects, $e \sim 10^{-5}$. Models with $e_0 \lesssim 10^{-4}$ should thus closely resemble $e_0 = 10^{-4}$ models. For $e \gtrsim 10^{-2}$, collisions lead to substantial fragmentation and mass loss from the numerical grid. Circularization is then less effective and growth is very slow (see Table 6). These calculations probably poorly approximate reality: dynamical friction between 1–100 m objects and smaller dust particles not included in our grid should reduce the velocities of 1–100 m objects on very short timescales³. We expect that these calculations would then more closely resemble models with smaller e_0 , if dust particles can grow back into 1 m bodies.

The final limitation of our model is the fragmentation algorithm. We adopt an energy-scaling fragmentation law, because other types of models have not been developed and tested for the low velocity conditions appropriate in the Kuiper Belt. Other scaling models seem to yield better results for main belt asteroids than do energy-scaling models, but these models assume that the collision can be approximated as a point-like impact on a large body (Davis *et al.* 1994; Durda *et al.* 1998; Ryan & Melosh 1998). This assumption is quite good for the high speed impacts, $\gtrsim 100\text{--}500 \text{ m s}^{-1}$, of strong, dense objects in the inner solar system. Point-like impacts are probably rare for the lower velocity collisions of weaker, low density objects like KBOs. Our consideration of KBOs with a large range of intrinsic strengths suggests that an improved fragmentation model would not change our results significantly.

³This problem does not occur in models with small e_0 , because the mass loss is $\lesssim 1\%$ of the initial mass.

4. DISCUSSION AND SUMMARY

In KL98 and this paper, we have developed a time-dependent planetesimal evolution code to calculate the formation of KBOs in a single annulus outside the orbit of Neptune. The computer program includes coagulation with realistic cross-sections, energy-scaling algorithms to treat cratering and disruption, and velocity evolution using the statistical expressions of Hornung *et al.* (1985). Our numerical solutions match standard analytic test cases and generally reproduce the results of other accretion and collision calculations (e.g., WS93; Davis & Farinella 1997).

Our calculations demonstrate that plausible models can satisfy current observations of the Kuiper Belt. Several Plutos and $\sim 10^5$ 50 km radius KBOs form in Minimum Mass Solar Nebulae with $e_0 \approx 10^{-3}$ on timescales of 20–40 Myr. Growth is more rapid in more massive nebulae and in planetesimal swarms with smaller initial velocities. The formation time is less sensitive to the initial size distribution, the intrinsic strength of KBOs, and other input parameters listed in Table 1.

Each Kuiper Belt model yields a cumulative size distribution with two main features. Objects with $r_i \lesssim 0.1$ km follow $N_C \propto r^{-q}$ with $q = 2.5$, as expected for collision fragments (Dohnanyi 1969; Williams & Wetherill 1994). Larger objects with $r_i \gtrsim 1$ –10 km follow a $q \approx 3$ power law over several orders of magnitude in radius. These slopes do not depend on M_0 , e_0 , S_0 , f_{KE} , and q_0 , among other input parameters. Kenyon & Luu (1999) compare these results with observations. Here, we note that the $q \approx 3$ power law for large bodies is identical to the observed slope, 3 ± 0.5 (Jewitt *et al.* 1998; Luu & Jewitt 1998; but see also Gladman *et al.* 1998).

Fragmentation and velocity evolution are important components in the formation of present day KBOs. Fragmentation produces a large reservoir of small bodies that damp the velocity dispersions of the large objects through dynamical friction. These processes allow a short runaway growth phase where 1 km objects grow into 100 km objects. Continued fragmentation and velocity evolution damp runaway growth by increasing the velocity dispersions of small objects. This evolution leaves $\sim 1\%$ – 2% of the initial mass in 50 km radius KBOs. The remaining mass is in 0.1–10 km radius objects. Fragmentation will gradually erode these smaller objects into dust grains that are removed from the Kuiper Belt on short timescales, $\sim 10^7$ yr (see Backman & Paresce 1993; Backman *et al.* 1995). Thus, 50 km radius KBOs comprise a small fraction of the original Kuiper Belt.

Fragmentation also limits the size of the largest object in the Kuiper Belt. The maximum radius ranges from $r_{max} \approx 450$ km for $S_0 = 10$ erg g $^{-1}$ to $r_{max} \gtrsim 3000$ km for $S_0 = 2 \times 10^6$ erg g $^{-1}$. Pluto formation sets a lower limit on the tensile strength of KBOs,

$$S_0 \geq 300 \text{ erg g}^{-1}.$$

These results suggest a refinement of our picture for KBO formation in the outer solar system. In KL98, we speculated that velocity perturbations due to the growth and outward migration of Neptune would limit the growth of KBOs at radii $\lesssim 1000$ km. Although this hypothesis is plausible (see, for example, Malhotra 1993; Morbidelli & Valsecchi 1997), our current models demonstrate that 50–1000 km radius KBOs form naturally at ~ 35 AU on timescales, $\tau_P \sim 10$ –100 Myr, comparable to the Neptune formation time. Although a few objects can reach 2000+ km radii on timescales of 2–3 τ_P , nearly all of the initial mass beyond 30 AU remains in small, 1 km radius objects that can be depleted by collisional disruption (Davis & Farinella 1997) or gravitational sculpting (Holman & Wisdom 1993) or both on timescales exceeding 100 Myr. This evolution can account for the observation of 50+ km KBOs in a currently small mass Kuiper Belt without intervention by Neptune.

Finally, our new results further support the notion that KBOs will form in other solar systems. The dusty circumstellar disks detected in many pre-main-sequence stars suggest masses of 1–100 M_E at distances of 30–100 AU (e.g., Sargent & Beckwith 1993; Beckwith & Sargent 1996; see also Close *et al.* 1997; Hogerheijde *et al.* 1997; Lay *et al.* 1997; Akeson *et al.* 1998; Stapelfeldt *et al.* 1998). KBOs with 50+ km radii can grow in this material as the central stars contract to the main-sequence if the disks are not too turbulent (see Cuzzi *et al.* 1993a, 1993b). Smaller, 1–10 km radius KBOs probably form in less massive pre-main-sequence disks. Our results also indicate that the growth of 100–1000 km radius KBOs is accompanied by substantial dust production, ~ 0.1 –1 M_E , in models with $M_0 \sim 10$ –100 M_E . This dust could be responsible for the ringlike structures observed in pre-main-sequence stars such as GG Tau (Roddier *et al.* 1996) and older main sequence stars such as ϵ Eri (Greaves *et al.* 1998) and HR 4796 (Jayawardhana *et al.* 1998; Koerner *et al.* 1998). The less massive disks in α Lyr, α PsA, and β Pic may also harbor KBOs if the dust masses are reasonably close to the ‘maximum’ masses inferred for these systems (Backman & Paresce 1993). In all of these stars, the dynamics and mass distribution of dust may well provide useful constraints on the properties of presumed KBOs. We hope to explore this possibility in future studies.

We thank B. Bromley for making it possible to run our code on the JPL Cray T3D ‘Cosmos’ and the HP Exemplar ‘Neptune’ and for a generous allotment of computer time through funding from the NASA Offices of Mission to Planet Earth, Aeronautics, and Space Science. Comments from A. Cameron, F. Franklin, M. Geller, M. Holman, S. Starrfield, and J. Wood greatly improved our presentation. We acknowledge G. Stewart for clarifying details of the WS93 calculations.

A. APPENDIX

A.1. Overview

As described in KL98, our accretion model assumes that planetesimals are a statistical ensemble of masses in a cylindrical annulus of width Δa and height H centered at a radius a from the Sun. The particles have horizontal $h_i(t)$ and vertical $v_i(t)$ velocity dispersions relative to an orbit with mean Keplerian velocity V_K (see Lissauer & Stewart 1993). We approximate the continuous distribution of particle masses with discrete batches having an integral number of particles $n_i(t)$ and total masses $M_i(t)$ (WS93). The average mass of a batch, $m_i(t) = M_i(t)/n_i(t)$, evolves with time as collisions add and remove bodies from the batch.

To compute the evolution of particle numbers and velocities in KL98, we solved the coagulation equation and a set of velocity evolution equations for all mass bins k during a time step δt . We assumed that bodies merge but do not fragment during collisions. We conserved kinetic energy in each collision and adopted a kinetic approximation to calculate velocity changes due to gas drag, dynamical friction, and viscous stirring. Our explicit algorithm for solving these equations reproduced standard tests and other published calculations.

In this paper, we consider collisions that produce mergers and debris. The coagulation equation is then:

$$\delta n_k = \delta t [\epsilon_{ij} A_{ij} n_i n_j - n_k A_{ik} n_i] + \delta n_{k,f} - \delta n_{k,gd} \quad (\text{A1})$$

$$\delta M_k = \delta t [\epsilon_{ij} A_{ij} n_i n_j m_k - n_k A_{ik} n_i m_k] + m_k \delta n_{k,f} - m_k \delta n_{k,gd} \quad (\text{A2})$$

where A_{ij} is the cross-section, $\epsilon_{ij} = 1/2$ for $i = j$ and $\epsilon_{ij} = 1$ for $i \neq j$. The four terms in A1–A2 represent (i) mergers of m_i and m_j into a body of mass $m_k = m_i + m_j - m_{e,ij}$, (ii) loss of m_k through mergers with other bodies, (iii) addition of m_k from debris produced by the collisions of other bodies, and (iv) loss of m_k by gas drag. We consider below the mass lost to small fragments $m_{e,ij}$. The second term in A1–A2 includes the possibility that a collision can produce debris but no merger (rebounds). As in KL98, we calculate the “gravitational range” of the largest bodies – $R_{g,i} = K_1 a R_{H,ii_{mid}} + 2ae_i$ (WS93) – where $K_1 = 2\sqrt{3}$ and $R_{H,ij} = [(m_i + m_j)/3M_\odot]^{1/3}$ is the mutual Hill radius. As in WS93, the isolated bodies are the N largest bodies that satisfy the summation, $\sum_{i_{min}}^{i_{max}} n_i R_{g,i} \geq \Delta a$. These isolated bodies cannot collide with one another but can collide with other lower mass

bodies.

As in KL98, we solve the complete set of evolution equations, A1–A2 above and A7–A8 from KL98, using an explicit method that limits the time step automatically to prevent large changes in the dynamical variables. Section 2 of the main text compares calculations at 1 AU with results from WS93. In the rest of this Appendix, we describe fragmentation algorithms (A.2) and updates to our velocity evolution algorithm (A.3).

A.2. Fragmentation

Algorithms for collision outcomes rely on comparisons between the kinetic energy of the two colliding planetesimals $Q_{c,ij}$ and the binding energy of the merged planetesimal $Q_{b,ij}$. The binding energy usually consists of an intrinsic tensile strength and the gravitational binding energy, $Q_{b,ij} = S_0 + Q_{g,ij}$. This ‘energy scaling’ approach is sometimes replaced by other scaling laws to model the structure of the colliding bodies more accurately. For example, Housen and collaborators (see Housen & Holsapple 1990; Housen *et al.* 1991; Holsapple 1993, 1994) describe a strain-rate scaling model to express the collision energy needed to disrupt a body in terms of its size and impact velocity. Davis *et al.* (1994) showed that both types of model can match observations of the asteroid belt in our solar system (see also Farinella *et al.* 1982; Davis *et al.* 1989; Williams & Wetherill 1994; Marzari *et al.* 1997).

In this paper, we adopt an energy scaling model. Energy scaling has two main advantages for calculating the fragmentation of Kuiper Belt objects. The wide use of this approach allows us to compare results with many previous calculations. Other models also seem inappropriate for the low velocity collisions anticipated in the Kuiper Belt. These models have been scaled for conditions in the inner Solar System, where collision velocities exceed 100 m s^{-1} (see Davis *et al.* 1994). The approximations made for these collision velocities fail when the impact velocity is smaller than $100\text{--}1000 \text{ m s}^{-1}$ (e.g., Housen & Holsapple 1990, p. 239). We expect velocities of $\lesssim 10 \text{ m s}^{-1}$ for most collisions in the Kuiper Belt (KL98), and thus cannot apply the Housen *et al.* (1990) and other sophisticated models in our calculations.

The output of any fragmentation algorithm is the mass of the merger remnant m_k and the mass distribution of the fragments. We assume $m_k = m_i + m_j - m_{e,ij}$, where $m_{e,ij}$ is the mass of fragments *ejected* from the merged planetesimal. We consider two approaches to compute $m_{e,ij}$. In the first case, we follow WS93 and set the impact velocity as

$$V_{I,ij}^2 = V_{ij}^2 + V_{e,ij}^2 \quad (\text{A3})$$

where V_{ij} is the relative velocity of the two colliding bodies (equation A12 of KL98) and $V_{e,ij}^2 = 2G(m_i + m_j)/(r_i + r_j)$ is the mutual escape velocity. The center of mass fragmentation energy $Q_{f,ij}$ and the gravitational binding energy $Q_{g,ij}$ per unit mass are

$$Q_{f,ij} = (K_2/2) m_i m_j V_{I,ij}^2 / (m_i + m_j)^2 \quad (\text{A4})$$

and

$$Q_{g,ij} = 0.6 G (m_i + m_j) / R_c \quad (\text{A5})$$

where R_c is the spherical radius of the combined body with mass $m_i + m_j$ and $K_2 = 0.5$ is a constant. We further define the fragmentation energy $E_{f,ij} = (m_i + m_j)Q_{f,ij}$.

WS93 and most other studies assume that collisions produce debris when (i) the impact velocity exceeds a threshold velocity, $V_{I,ij} > V_f$, and (ii) the amount of ejected mass exceeds a threshold value, $m_{e,ij} > 10^{-8}(m_i + m_j)$. The mass ejected in the collision is derived from simple energy considerations. The collision *disrupts* the merged object if the collision energy exceeds the binding energy, $Q_{f,ij} > Q_{g,ij} + S_0$, where S_0 is the impact strength. In most of their calculations, WS93 further require that the mass fragmented by the impact exceed half of the mass of the merged object, $m_{f,ij} > 0.5(m_i + m_j)$, where the fragmented mass is (Greenberg *et al.* 1978, 84):

$$m_{f,ij} = Q_{f,ij} / Q_c, \quad (\text{A6})$$

and Q_c is the crushing energy. If both conditions for ‘‘catastrophic disruption’’ are met, the collision produces a large fragment with mass (Fujiwara *et al.* 1977; see also Fujiwara 1980, Housen & Holsapple 1990):

$$m_{L,ij} = 0.5 (m_i + m_j) (Q_{m,ij} / (Q_{g,ij} + Q_b))^{-1.24}, \quad (\text{A7})$$

and numerous smaller fragments. In all cases, $m_{L,ij} < 0.5 (m_i + m_j)$.

If the conditions for catastrophic disruption are not met, the collision produces a large body with $m_k \approx m_i + m_j$ and numerous small fragments with total mass $m_{f,ij}$ (A6). WS93 assume that the amount of the fragmented mass that escapes the merged body is

$$m_{e,ij} = K_3 m_{f,ij} V_{e,ij}^{-2.25} \quad (\text{A8})$$

where $K_3 = 3 \times 10^6 \text{ (cm s}^{-1}\text{)}^{2.25}$ is a constant (see also Gault *et al.* 1963; Greenberg *et al.* 1978). The mass of the largest fragment in this case is

$$m_{L,ij} = 0.2 m_{e,ij} . \quad (\text{A9})$$

In WS93, the mass distribution of the debris depends on the method of fragmentation. We simplify this procedure and adopt a single power law distribution for both methods:

$$\delta n_k = C_k (m_1^{-b} - m_2^{-b}) \quad (\text{A10})$$

where $b = (1 + m_{L,ij}/m_{e,ij})^{-1}$, $C_k = m_{L,ij}^b$, $m_1 = (m_k m_{k-1})^{1/2}$, and $m_2 = (m_k m_{k+1})^{1/2}$ (Greenberg *et al.* 1978). Tests show that this distribution produces results similar to those of WS93 when we assume that the velocity of the escaping fragments equals the relative velocity of the colliding planetesimals, V_{ij} (see section 2).

As a comparison to the WS93 fragmentation algorithm, we consider the Davis *et al.* (1985; Greenberg *et al.* 1978, 1984; Davis *et al.* 1994) approach. We adopt their energy scaling formula and write the strength (in erg g^{-1}) of a planetesimal as:

$$S = S_0 + \frac{4\pi K_4 G \rho_0 R_c^2}{15} , \quad (\text{A11})$$

where K_4 is a constant. We adopt $K_4 = 1$ in the absence of any useful estimates for Kuiper Belt objects; Davis *et al.* (1985, 1994) consider $K_4 = 1$ –100 for collisional evolution in the asteroid belt (see also Housen & Holsapple 1990). Davis *et al.* assume that the ejecta receive a fixed fraction $f_{KE} Q_{f,ij}$ of the impact energy and have a power law mass-velocity distribution,

$$f(> v) \propto (v/v_c)^{-\alpha v} , \quad (\text{A12})$$

where v_c is a reference velocity. The impact energy needed to disrupt the planetesimal and accelerate 50% of the fragments to escape velocity follows from integration of (A12) and energy conservation (Davis *et al.* 1985):

$$Q_d = S \left(\frac{\alpha_V 0.5^{1 + 2/\alpha_V}}{f_{KE}(\alpha_V - 2)} \right). \quad (\text{A13})$$

Davis *et al.* assume that collisions produce debris when the impact velocity exceeds a threshold, $V_{I,ij} > V_f$. We also adopt the WS93 threshold for the ejected mass, $m_{e,ij} > 10^{-8}(m_i + m_j)$. The collision disrupts the colliding bodies if $Q_{m,ij} > Q_d$. If this condition is met, the total mass lost is:

$$m_{e,ij} = 0.5 (m_i + m_j) (Q_{m,ij}/Q_d)^{0.5\alpha_V}, \quad (\text{A14})$$

while the mass of the largest fragment is the smaller of

$$m_{L,ij} = \begin{cases} 0.5 (m_i + m_j) (Q_{m,ij}/Q_d)^{1-\alpha_V} \\ 0.2 m_{e,ij} \end{cases} \quad (\text{A15})$$

If the collision does not disrupt the merged planetesimal, the mass in fragments is simply $m_{f,ij}$ from (A6). To estimate the fraction of this mass that escapes, we follow the Davis *et al.* (1985) derivation of Q_d and integrate the mass distribution over velocity:

$$m_{e,ij} = \left(\frac{f_{KE} (\alpha_V - 2) m_j V_{I,ij}^2}{\alpha_V m_{f,ij} V_{e,ij}^2} \right)^{0.5\alpha_V} \quad (\text{A16})$$

The mass of the largest fragment is then $m_{L,ij} = 0.2 m_{e,ij}$ as before. We calculate the mass distribution of the fragments as in (A10) and assume that all fragments have the same kinetic energy per unit mass.

Unlike WS93, Davis *et al.* allow for ‘rebounds,’ where the colliding bodies do not merge into a single body. We follow Barge & Pellat (1992) and define the rebound velocity as

$$V_{reb,ij}^2 = \frac{2(1 - c_R^2)}{c_R^2} V_{e,ij}^2 \quad (\text{A17})$$

where c_R is the coefficient of restitution. In most applications, c_R takes on separate values for collisions with impact velocities above and below the fragmentation threshold:

$$c_R = \begin{cases} c_1 & V_{I,ij} < V_f \\ c_2 & V_{I,ij} \geq V_f \end{cases} \quad (\text{A18})$$

With these definitions, collisions with $V_{I,ij} < V_{reb,ij}$ produce mergers and debris; collisions with $V_{I,ij} > V_{reb,ij}$ produce debris but no merger. We assume that rebounds conserve energy and that the velocity difference between bodies after the collision is

$$(v_i - v_j)_{after} = c_R(v_i - v_j)_{before}. \quad (\text{A19})$$

Tests of the coagulation code indicate that this prescription yields results almost identical to a prescription where we assume that the particle velocities are not changed by the rebound.

In addition to the tests described in section 2, we repeat the collisional evolution of KBOs described in Davis & Farinella (1997). With suitable modifications to our algorithms for the collision cross-section and velocity evolution, we reproduce their results to $\sim 10\%$ – 20% .

A.3. Velocity evolution

Our procedure for treating the evolution of the horizontal h_i and vertical v_i components of the velocity dispersion follows the kinetic formalism developed by Hornung *et al.* (1985) and Barge & Pellat (1990, 1991, 1992). In KL98, we adopted the WS93 expressions for dynamical friction and viscous stirring due to long range encounters and reformulated the Barge & Pellat (1990, 1991) expressions for inelastic collisions in terms of e and i (see equations A19–A22 of KL98). We verified that our algorithm for computing the velocity evolution achieved the equilibrium value for the ratio of the vertical to the horizontal velocity $\beta = i/e = 0.6$ (Hornung *et al.* 1985) and generally reproduced the velocity evolution of the WS93 Earth calculation.

In this paper, we make two modifications to our treatment of the velocity evolution and clarify our treatment of velocity evolution at low velocities. We assume that rebound collisions do not contribute to dynamical friction and viscous stirring for inelastic collisions (equations A21 and A22 of KL98). With this assumption, the orbits of low mass objects do not circularize when their velocity dispersion exceeds the rebound velocity (equation A17 above). This behavior slows down the growth time of massive objects, because the collision cross-section remains in the high velocity limit.

Although the kinetic prescription of Hornung *et al.* (1985) accurately represents dynamical evolution at high particle velocities, it fails as the particle velocity approaches the Hill velocity $v_{H,ij} = \Omega R_{H,ij}$ (Ida 1990; Barge & Pellat 1991; WS93). Ida (1990) used N -body calculations to derive the appropriate behavior at low particle velocities, $V_{ij} < 2\text{--}5$

$v_{H,ij}$. We generally reproduce Ida’s (1990) results if we adopt

$$\left(\frac{de_{vs,i}^2}{dt}\right)_{lv} = \left(\frac{e_i^2 + e_j^2}{e_{ij,lv}}\right) \left(\frac{de_{vs,i}^2}{dt}\right)_{hv}, \quad \left(\frac{di_{vs,i}^2}{dt}\right)_{lv} = \left(\frac{e_i^2 + e_j^2}{e_{ij,lv}}\right)^2 \left(\frac{di_{vs,i}^2}{dt}\right)_{hv} \quad (\text{A20})$$

for viscous stirring and

$$\left(\frac{de_{df,i}^2}{dt}\right)_{lv} = \left(\frac{e_i^2 + e_j^2}{e_{ij,lv}}\right)^2 \left(\frac{de_{df,i}^2}{dt}\right)_{hv}, \quad \left(\frac{di_{df,i}^2}{dt}\right)_{lv} = \left(\frac{e_i^2 + e_j^2}{e_{ij,lv}}\right)^2 \left(\frac{di_{df,i}^2}{dt}\right)_{hv} \quad (\text{A21})$$

for dynamical friction (see also Barge & Pellat 1991, WS93). In both equations, the ‘hv’ subscript indicates the appropriate high velocity expression from KL98 (equations A19 and A20) and $e_{ij,lv}$ is the value of $e_i^2 + e_j^2$ at $V_{ij} = V_{lv} v_{H,ij}$. These equations yield constant timescales for dynamical friction and the inclination component of viscous stirring (Ida 1990; Figure 10). The timescale for the eccentricity component of viscous stirring varies as e^2 at low velocity (Ida 1990).

We describe the sensitivity of the velocity evolution to the choice of V_{lv} in Sec. 2. Any $V_{lv} \gtrsim 2$ slows down velocity evolution significantly, because the most massive particles in our test calculations have $V_{ij} \lesssim 0.3\text{--}0.5 v_{H,ij}$. The velocity changes are then ~ 25 times smaller for viscous stirring and ~ 500 times smaller for dynamical friction (see also Ida 1990, Barge & Pellat 1991, WS93). Our results are not very sensitive to V_{lv} for $2 \lesssim V_{lv} \lesssim 5$: the velocity evolution slows down gradually as V_{lv} increases from 2 to 5 (see Sec. 2). We adopt the middle of Ida’s (1990) range, $V_{lv} = 3.5$, in our Kuiper Belt calculations. For comparison, WS93 adopt $V_{lv} = 2$; Barge & Pellat 1991 adopt $V_{lv} = 0.8$ for viscous stirring and $V_{lv} = 2.6$ for dynamical friction.

In many of our Kuiper Belt calculations, the velocity of the largest bodies approaches zero due to collisional damping, dynamical friction, and fragmentation. To avoid divergences in the stirring rates from long-range encounters, we adopt a minimum horizontal velocity of 10^{-3} m s^{-1} and a minimum vertical velocity of $5.3 \times 10^{-4} \text{ m s}^{-1}$. This ‘floor’ to the velocity evolution maintains the appropriate β_{ij} for collisions with $V_{ij} > V_{lv} v_{H,ij}$ and allows larger time steps for the brief interval when growth is rapid and the viscous stirring rate is small. Tests show that the growth rate of the largest bodies does not depend on the values for these limits. Lower values for the ‘floor’ result in somewhat higher velocities for the small mass objects, but these changes are small. Once viscous stirring begins to dominate collisional cooling, the velocities of all bodies increase above our ‘floor’ values.

Finally, to reduce the computation time of our velocity evolution algorithm, we approximate the I , J , and K integrals in equations A19–A22 of KL98 with polynomial expressions derived using *Mathematica*⁴. Our results match the integral expressions to better than 1 part in 10^3 for $\beta_{ij} = 0$ –1. Expressions ready for use in a computer calculation appear below.

$$I_r = 14.1439 + 0.0675783/\beta_{ij} + \beta_{ij} * (3.86566 + \beta_{ij} * (-6.5623 + \beta_{ij} * (12.8084 + \beta_{ij} * (-9.93223 + 2.94993 * \beta_{ij})))) \quad (\text{A21})$$

$$I_\theta = 2.32693 + 0.0337724/\beta_{ij} + \beta_{ij} * (1.80115 + \beta_{ij} * (-3.3792 + \beta_{ij} * (5.78079 + \beta_{ij} * (-4.43822 + 1.32431 * \beta_{ij})))) \quad (\text{A22})$$

$$I_z = -0.00137043 + \beta_{ij} * (0.121347 + \beta_{ij} * (7.27632 + \beta_{ij} * (6.32281 + \beta_{ij} * (4.98011 - 1.36123 * \beta_{ij})))) \quad (\text{A23})$$

$$J_r = -4.21891 + \beta_{ij} * (-0.762162 + \beta_{ij} * (37.2078 + \beta_{ij} * (-97.5891 + \beta_{ij} * (120.258 + \beta_{ij} * (-72.0619 + \beta_{ij} * (14.8515 + 1.57744 * \beta_{ij})))))) \quad (\text{A24})$$

$$J_\theta = -1.90771 + \beta_{ij} * (13.8618 + \beta_{ij} * (-30.8032 + \beta_{ij} * (47.3479 + \beta_{ij} * (-49.4466 + \beta_{ij} * (32.4446 + \beta_{ij} * (-11.7370 + 1.72263 * \beta_{ij})))))) \quad (\text{A25})$$

$$J_z = 6.12664 + \beta_{ij} * (-13.1003 + \beta_{ij} * (-6.3946 + \beta_{ij} * (50.1757 + \beta_{ij} * (-70.6068 + \beta_{ij} * (39.2953 + \beta_{ij} * (-2.86619 - 3.37452 * \beta_{ij})))))) \quad (\text{A26})$$

⁴Mathematica v3.0.2 ©1988-1997 Wolfram Research, Inc.

$$\begin{aligned}
K_r = & 3.16452 + \beta_{ij} * (0.0149191 + \beta_{ij} * (-1.73044 + \beta_{ij} * (1.55516 \\
& + \beta_{ij} * (1.08438 + \beta_{ij} * (-3.55476 + \beta_{ij} * (2.91763 \\
& - 0.841079 * \beta_{ij})))))) \tag{A27}
\end{aligned}$$

$$\begin{aligned}
K_\theta = & 2.96882 + 0.135176/\beta_{ij} + \beta_{ij} * (7.13193 + \beta_{ij} * (-24.1086 \\
& + \beta_{ij} * (39.3287 + \beta_{ij} * (-35.5738 + \beta_{ij} * (15.0527 \\
& + \beta_{ij} * (-0.327693 - 1.25529 * \beta_{ij})))))) \tag{A28}
\end{aligned}$$

$$\begin{aligned}
K_z = & 6.13154 + 0.13519/\beta_{ij} + \beta_{ij} * (-6.70136 + \beta_{ij} * (4.49227 \\
& + \beta_{ij} * (-6.53516 + \beta_{ij} * (19.317 + \beta_{ij} * (-29.5368 \\
& + \beta_{ij} * (21.0967 - 5.78973 * \beta_{ij})))))) \tag{A29}
\end{aligned}$$

REFERENCES

- Akeson, R. L., Koerner, D. W., & Jensen, E. L. N. 1998, *ApJ*, 505, 358
- Bailey, M. 1994, In *Asteroids, Comets, Meteors 1993*, eds. A. Milani, M. DiMartino, and A. Cellino (Kluwer Academic Publishers, Dordrecht), pp. 443 - 459.
- Backman, D. E., & Paresce, F. 1993, in *Protostars and Planets III*, eds. E. H. Levy & J. I. Lunine, Tucson, Univ of Arizona, p. 1253
- Backman, D. E., Dasgupta, A., & Stencel, R. E. 1995, *ApJ*, 450, L35
- Barge, P., & Pellat, R. 1990, *Icarus*, 85, 481
- Barge, P., & Pellat, R. 1991, *Icarus*, 93, 270
- Barge, P., & Pellat, R. 1993, *Icarus*, 104, 79
- Beckwith, S. V. W., & Sargent, A. I. 1996, *Nature*, 383, 139
- Beckwith, S. V. W., Sargent, A. I., Chini, R., & Güsten, R. 1990, *AJ*, 99, 924
- Boss, A. P. 1997, *Science*, 276, 1836
- Close, L. M., Roddier, F., Hora, J. L., Graves, J. E., Northcott, M., Roddier, C., Hoffman, W. F., Dayal, A., Fazio, G. G., & Deutsch, L. K. 1997, *ApJ*, 489, 210
- Cuzzi, J. N., Dobrovolskis, A. R., & Champney, J. M. 1993, *Icarus*, 100, 102
- Cuzzi, J. N., Dobrovolskis, A. R., & Champney, J. M. 1993, *Icarus*, 106, 102
- Davis, D. R., Chapman, C. R., Weidenschilling, S. J., & Greenberg, R. 1985, *Icarus*, 62, 30
- Davis, D. R., & Farinella, P. 1997. *Icarus*, 125, 50
- Davis, D. R., Ryan, E. V., & Farinella, P. 1994, *Planet. Space Sci.*, 42, 599
- Davis, D. R., Weidenschilling, S. J., Farinella, P., Paolicchi, P., & Binzel, R. P. 1989, in *Asteroids II*, edited by R. P. Binzel, T. Gehrels, & M. S. Matthews, Tucson, Univ. of Arizona Press, p. 805
- Dohnanyi, J. W. 1969, *J. Geophys. Res.*, 74, 2531
- Duncan, M. J., Levison, H. F., & Budd, S. M. 1995, *AJ*, 110, 3073
- Durda, D. D., Greenberg, R., & Jedicke, P. 1998, *Icarus*, 135, 431

- Farinella, P., Paolicchi, P., & Zappalá, V. 1992, A&A, 253, 604
- Fernández, J. A., & Ip, W.-H. 1981, Icarus, 47, 470
- Fernández, J. A., & Ip, W.-H. 1984, Icarus, 58, 109
- Fujiwara, A. 1980, Icarus, 41, 356
- Gault, D. E., Shoemaker, E. M., & Moore, H. J. 1963, NASA TN, 1767
- Gladman, B., & Kavelaars, J. J. 1997, A&A, 317, L35
- Gladman, B., Kavelaars, J. J., Nicholson, P. D., Loredo, T. J., & Burns, J. A. 1998, AJ, 116, 2042
- Goldreich, P., & Ward, W. R. 1973, ApJ, 183, 1051
- Greaves, J. S. *et al.* 1998, ApJ, 506, L133
- Greenberg, R., Wacker, J. F., Hartmann, W. K., & Chapman, C. R. 1978, Icarus, 35, 1
- Greenberg, R., Weidenschilling, S. J., Chapman, C. R., & Davis, D. R. 1984, Icarus, 59, 87
- Hartmann, L., Calvet, N., Gullbring, E., & D'Alessio, P. 1998, ApJ, 495, 385
- Hayashi, C. 1981, Prog Theor Phys Suppl, 70, 35
- Hogerheijde, M. R., van Langevelde, H. J., Mundy, L. G., Blake, G. A., & van Dishoeck, E. F. 1997, ApJ, 490, L99
- Holman, M. J., & Wisdom, J. 1993, AJ, 105, 1987
- Holsapple, K. A. 1993, Ann. Rev. Earth Planet. Sci., 21, 333
- Holsapple, K. A. 1994, Planet. Space Sci., 42, 1067
- Housen, K., & Holsapple, K. 1990, Icarus, 84, 226
- Housen, K., Schmidt, R. M., & Holsapple, K. 1991, Icarus, 94, 180
- Hornung, P., Pellat, R., & Barge, P. 1985, Icarus, 64, 295
- Ida, S. 1990, Icarus, 88, 129
- Ip, W.-H. 1989, Icarus, 80, 167
- Irwin, M., Tremaine, S., & Żytkow, A. N. 1995, AJ., 110, 3082

- Jayawardhana, R. *et al.* 1998, ApJ, 503, L79
- Jedicke, P., & Metcalfe, T. S. 1998, Icarus, 131, 245
- Jewitt, D., & Luu, J. 1993, Nature, 362, 730
- Jewitt, D., & Luu, J. 1995, AJ, 109, 1867
- Jewitt, D., Luu, J., & Chen, J. 1996, AJ, 112, 1225
- Jewitt, D., Luu, J. X., & Trujillo, C. 1998, AJ, 115, 2125
- Kenyon, S. J., & Luu, J. X. 1998, AJ, 115, 2136 (KL98)
- Kenyon, S. J., & Luu, J. X. 1999, ApJL, submitted
- Kim, S.-H., Martin, P. G., & Hendry, P. D. 1994, ApJ, 422, 164
- Koerner, D. W., Ressler, M. E., Werner, M. W., & Backman, D. E. 1998, ApJ, 503, L83
- Kolvoord, R. A. & Greenberg, R. 1992, Icarus, 98, 2
- Lay, O. P., Carlstrom, J. E., & Hills, R. E. 1997, ApJ, 489, L917
- Lazzaro, D., Sicardy, B., Roques, F., & Greenberg, R. 1994, Icarus, 108, 59
- Levison, H. F., & Duncan, M. J. 1993, ApJ, 406, L35
- Li, A., & Greenberg, J. M. 1997, A&A, 323, 566
- Lissauer, J. J., & Stewart, G. R. 1993, In *Protostars and Planets III*, edited by E. H. Levy and J. I. Lunine, U. of Arizona Press, Tucson, 1061
- Lissauer, J. J., Pollack, J. B., Wetherill, G. W., & Stevenson, D. J. 1996. "Formation of the Neptune System." In Neptune and Triton, eds. D. P. Cruikshank, M. S. Matthews, and A. M. Schumann (U. of Arizona Press, Tucson, pp. 37 - 108.
- Luu, J. X., & Jewitt, D. 1998, ApJ, 502, L91
- Luu, J. X., Marsden, B., Jewitt, D., Trujillo, C. A., Hergenother, C. W., Chen, J., & Offutt, W. B. 1997, Nature, 387, 573
- Malhotra, R. 1993, Nature, 365, 819
- Malhotra, R. 1995, AJ, 110, 420

- Marzari, F., Farinella, P., Davis, D. R., Scholl, H., Bagatin, A. C. 1997, *Icarus*, 125, 39
- Morbidelli, A., & Valsecchi, G. B. 1997, *Icarus*, 128, 464
- Ohtsuki, K., & Nakagawa, Y. 1988, *Prog Theor Phys (Suppl)*, 96, 239
- Ohtsuki, K., Nakagawa, Y., & Nakazawa, K. 1990, *Icarus*, 83, 205
- Osterloh, M. & Beckwith, S. V. W. 1994, *ApJ*, 439, 288
- Pollack, J. B. 1984, *ARA&A*, 22, 389
- Pollack, J. B., Hubickyj, O., Bodenheimer, P., Lissauer, J. J., Podolak, M., & Greenzweig, Y. 1996, *Icarus*, 124, 62
- Roddiar, C., Roddiar, F., Northcott, M. J., Graves, J. E. & Jim, K. 1996, *ApJ*, 463, 326
- Roques, F., Scholl, H., Sicardy, B., & Smith, B. A. 1994, *Icarus*, 108, 37
- Russell, S. S., Srinivasan, G., Huss, G. R., Wasserburg, G. J., & Macpherson, G. J. 1996, *Science*, 273, 757
- Ryan, E. V., & Melosh, H. J. 1998, *Icarus*, 133, 1
- Safronov, V. S. 1969, *Evolution of the Protoplanetary Cloud and Formation of the Earth and Planets*, Nauka, Moscow [Translation 1972, NASA TT F-677]
- Sargent, A. I., & Beckwith, S. V. W. 1993, *Phy Tod*, 46, 22
- Spaute, D., Weidenschilling, S. J., Davis, D. R., & Marzari, F. 1991, *Icarus*, 92, 147
- Stapelfeldt, K. R., Krist, J. E., Ménard, F., Bouvier, J., Padgett, D. K., & Burrows, C. J. 1998, *ApJ*, 502, L65
- Stern, S. A. 1995, *AJ*, 110, 856
- Stern, S. A. 1996, *AJ*, 112, 1203
- Stern, S. A., & Colwell, J. E. 1997a, *AJ*, 114, 841
- Stern, S. A., & Colwell, J. E. 1997b, *ApJ*, 490, 879
- Tremaine, S. 1990, In *Baryonic Dark Matter*, edited by D. Lynden-Bell & G. Gilmore, Kluwer, Dordrecht, p. 37
- Ward, W. R., & Hahn, J. M. 1998, *AJ*, 116, 489

- Weidenschilling, S. J. 1977, *Astrophys Sp Sci*, 51, 153
- Weidenschilling, S. J. 1997, *Icarus*, 127, 290
- Weidenschilling, S. J., Spaute, D., Davis, D. R., Marzari, F., & Ohtsuki, K. 1997, *Icarus*, 128, 429
- Wetherill, G. W. 1990, *Icarus*, 88, 336
- Wetherill, G. W., & Stewart, G. R. 1989. *Icarus* 77, 300 - 357.
- Wetherill, G. W., & Stewart, G. R. 1993, *Icarus*, 106, 190 (WS93)
- Williams, D. R., & Wetherill, G. W. 1994, *Icarus*, 107, 117
- Williams, I. P., O'Ceallaigh, D. P., Fitzsimmons, A., & Marsden, B. G. 1995, *Icarus*, 116, 180
- Wurm, G., & Blum, J. 1998, *Icarus*, 132, 125

This preprint was prepared with the AAS L^AT_EX macros v4.0.

TABLE 1. Basic Model Parameters

Parameter	Symbol	1 AU Models	35 AU Models
Width of annulus	δa	0.17 AU	6 AU
Initial velocity	V_0	4.7 m s ⁻¹	0.45–45 m s ⁻¹
Particle mass density	ρ_0	3 g cm ⁻³	1.5 g cm ⁻³
Relative gas velocity	η	60 m s ⁻¹	30 m s ⁻¹
Time step	δt	0.5 yr	1–250 yr
Number of mass bins	N	70–400	64–256
Mass spacing of bins	δ	1.1–2.0	1.25–2.0
Minimum velocity for cratering	V_f	50 m s ⁻¹	1 cm s ⁻¹
Impact strength	S_0	10 ⁷ erg g ⁻¹	2 × 10 ⁶ erg g ⁻¹
Crushing energy	Q_c	10 ⁸ erg g ⁻¹	5 × 10 ⁷ erg g ⁻¹
Fraction of KE in ejecta	f_{KE}	0.10	0.05
Coefficient of restitution	c_1	10 ⁻⁷	10 ⁻²
Coefficient of restitution	c_2	10 ⁻⁷	10 ⁻³

TABLE 2. Model Results at 1 AU

Time (yr)	$\delta = 1.12$			$\delta = 1.25$			$\delta = 1.4$			$\delta = 2.0$		
	r_{max}	$m(r_{max})$	N	r_{max}	$m(r_{max})$	N	r_{max}	$m(r_{max})$	N	r_{max}	$m(r_{max})$	N
1.0×10^3	26.8	2.4×10^{20}	7	25.7	2.1×10^{20}	5	23.6	1.6×10^{20}	33	19.1	8.7×10^{19}	646
7.1×10^3	326.0	4.4×10^{23}	2	304.1	3.5×10^{23}	1	284.1	2.9×10^{23}	1	153.0	4.5×10^{22}	10
1.0×10^4	525.2	1.8×10^{24}	1	509.3	1.7×10^{24}	2	488.6	1.5×10^{24}	1	314.8	3.9×10^{23}	8
2.0×10^4	952.2	1.1×10^{25}	3	976.5	1.2×10^{25}	1	873.2	8.4×10^{24}	1	801.5	6.5×10^{24}	5
6.3×10^4	1450.4	3.8×10^{25}	1	1470.2	4.0×10^{25}	2	1446.0	3.8×10^{25}	5	1675.7	6.1×10^{25}	1
1.0×10^5	1931.4	9.1×10^{25}	1	1780.5	7.1×10^{25}	1	1830.7	7.7×10^{25}	3	1915.0	8.8×10^{25}	1
1.2×10^5	1962.7	9.5×10^{25}	1	1801.4	7.4×10^{25}	2	1888.2	8.5×10^{25}	1	1948.0	9.3×10^{25}	1

Notes to Table 2.

These results are for the WS93 fragmentation algorithm. The columns list the mass and radius of the N largest bodies, $m(r_{max})$ in g and r_{max} in km, as a function of time for four values of the mass spacing, δ .

TABLE 3. Model Results at 1 AU

Time (yr)	$\delta = 1.25$			$\delta = 1.4$			$\delta = 2.0$		
	r_{max}	$m(r_{max})$	N	r_{max}	$m(r_{max})$	N	r_{max}	$m(r_{max})$	N
1.0×10^3	25.5	2.1×10^{20}	7	23.6	1.6×10^{20}	33	19.1	8.7×10^{19}	646
7.1×10^3	283.1	2.9×10^{23}	5	257.4	2.1×10^{23}	5	159.3	5.1×10^{22}	44
1.0×10^4	523.3	1.9×10^{24}	1	474.9	1.3×10^{24}	2	364.4	6.1×10^{23}	1
2.0×10^4	948.1	1.1×10^{25}	1	948.1	1.1×10^{25}	1	812.5	6.7×10^{24}	2
6.3×10^4	2068.8	1.1×10^{26}	1	1739.5	6.6×10^{25}	1	1479.2	4.1×10^{25}	4
1.0×10^5	2316.6	1.6×10^{20}	1	2129.6	1.0×10^{26}	1	1724.8	6.5×10^{25}	7
1.2×10^5	2407.3	1.8×10^{20}	1	2212.6	1.2×10^{26}	1	1793.9	7.3×10^{25}	7

Notes to Table 3.

These results are for the Davis *et al.* fragmentation algorithm. The columns list the mass and radius of the N largest bodies, $m(r_{max})$ in g and r_{max} in km, as a function of time for three values of the mass spacing, δ .

TABLE 4. Fragmentation Results at 100 Myr for $e_0 = 10^{-3}$ (No Velocity Evolution)

M_0 (M_E)	c_R	r_0 (m)	$r_{95\%}$ (km)	r_5 (km)	r_{max} (km)	$N(r_{max})$	τ_P (Myr)
1	10^{-5}	80	0.3	0.6	0.6	2660	2764
3	10^{-5}	80	1.0	1.6	1.8	46	919
10	10^{-5}	80	3.7	5.8	7.0	2034	276
30	10^{-5}	80	657.2	337.2	1006.0	3	92
100	10^{-5}	80	587.8	451.7	1022.5	1	27.6
1	10^{-2}	80	0.3	0.6	0.6	1223	2803
3	10^{-2}	80	1.0	1.6	1.9	2	937
10	10^{-2}	80	3.5	5.8	6.6	61	280
30	10^{-2}	80	659.3	333.9	1080.1	1	93.7
100	10^{-2}	80	659.4	477.6	1133.4	2	27.6

Notes to Table 4.

The columns list $r_{95\%}$ (95% of the mass is contained in objects with radius less than $r_{95\%}$), r_5 (the radius where the cumulative number of objects is 10^5), r_{max} (the radius of the largest object), $N(r_{max})$ (the number of objects with radius r_{max}), and τ_P (the timescale to produce 1000 km objects) as functions of the initial mass in the annulus (M_0), the coefficient of restitution (c_R), and the initial radius of the largest object (r_0).

TABLE 5. Fragmentation Results at 100 Myr for $e_0 = 10^{-3}$ (Limited Velocity Evolution)

M_0 (M_E)	c_R	r_0 (m)	$r_{95\%}$ (km)	r_5 (km)	r_{max} (km)	$N(r_{max})$	τ_P (Myr)
1	10^{-2}	80	0.3	0.6	0.6	1084	2150
3	10^{-2}	80	1.0	1.6	1.9	3	720
10	10^{-2}	80	3.9	6.4	7.5	31	216
30	10^{-2}	80	656.1	333.2	1089.9	1	72.1
100	10^{-2}	80	735.0	537.4	1240.4	4	21.6

Notes to Table 5.

The columns list $r_{95\%}$ (95% of the mass is contained in objects with radius less than $r_{95\%}$), r_5 (the radius where the cumulative number of objects is 10^5), r_{max} (the radius of the largest object), $N(r_{max})$ (the number of objects with radius r_{max} , and τ_P (the timescale to produce 1000 km objects) as functions of the initial mass in the annulus (M_0), the coefficient of restitution (c_R), and the initial radius of the largest object (r_0).

TABLE 6. Fragmentation Results for $c_R = 10^{-2}$ (Complete Velocity Evolution)

M_0 (M_E)	e_0	r_0 (m)	$r_{95\%}$ (km)	r_5 (km)	r_{max} (km)	$N(r_{max})$	τ_P (Myr)
1	10^{-4}	80	1.6	22.1	1000.1	1	447.8
10	10^{-4}	80	0.8	49.8	1000.2	4	20.1
1	10^{-3}	80	3.5	26.0	997.2	1	892.7
3	10^{-3}	80	2.5	32.7	1000.2	1	183.6
10	10^{-3}	80	1.8	52.6	1036.8	1	36.5
30	10^{-3}	80	1.8	73.0	1002.6	1	10.4
100	10^{-3}	80	1.8	115.1	1143.1	1	2.6
10	10^{-2}	80	17.7	50.4	1000.2	1	428.3
100	10^{-2}	80	11.3	89.0	1004.3	5	25.4

Notes to Table 6.

The columns list $r_{95\%}$ (95% of the mass is contained in objects with radius less than $r_{95\%}$), r_5 (the radius where the cumulative number of objects is 10^5), r_{max} (the radius of the largest object), $N(r_{max})$ (the number of objects with radius r_{max}), and τ_P (the timescale to produce 1000 km objects) as functions of the initial mass in the annulus (M_0), the coefficient of restitution (c_R), and the initial radius of the largest object (r_0).

TABLE 7. Fragmentation Results as a Function of Strength and Mass Spacing

M_0 (M_E)	e_0	δ	S_0 (erg g $^{-1}$)	τ_f (Myr)	r_5 (km)	r_{max}
10	10^{-4}	2.0	10^1	50	55.4	468.2
10	10^{-4}	2.0	10^1	100	55.4	473.4
10	10^{-4}	2.0	10^2	50	54.7	670.6
10	10^{-4}	2.0	10^2	100	54.7	776.1
10	10^{-4}	2.0	10^3	50	55.3	1200.8
10	10^{-4}	2.0	10^3	100	55.3	1210.6
10	10^{-4}	2.0	10^4	50	55.8	1584.8
10	10^{-4}	2.0	10^4	100	55.8	1605.0
10	10^{-4}	2.0	10^5	50	62.8	2002.6
10	10^{-4}	2.0	10^5	100	63.2	2331.3
10	10^{-4}	1.4	10^4	50	50.1	1506.4
10	10^{-4}	1.4	10^4	100	50.1	1706.2
10	10^{-4}	1.4	10^5	50	50.1	1525.4
10	10^{-4}	1.4	10^5	100	50.2	2254.8
10	10^{-4}	1.4	2×10^6	50	50.2	1552.6
10	10^{-4}	1.4	2×10^6	100	50.5	2382.8
10	10^{-3}	2.0	10^4	50	47.0	1621.0
10	10^{-3}	2.0	10^4	100	47.1	2038.2
10	10^{-3}	2.0	2×10^6	50	52.8	1452.9
10	10^{-3}	2.0	2×10^6	100	53.2	2019.2
10	10^{-3}	1.4	10^4	50	55.5	1381.4
10	10^{-3}	1.4	10^4	100	55.6	1834.9
10	10^{-3}	1.4	2×10^6	50	52.8	1452.9
10	10^{-3}	1.4	2×10^6	100	53.2	2019.2
10	10^{-3}	1.25	2×10^6	50	45.6	2309.1
10	10^{-3}	1.25	2×10^6	100	45.6	3333.0

Notes to Table 7.

The columns list r_5 (the radius where the cumulative number of objects is 10^5) and r_{max} (the radius of the largest object), $N(r_{max})$ (the number of objects with radius r_{max} at two times, τ_f , as functions of the initial mass in the annulus (M_0), the initial eccentricity (e_0) the mass spacing (δ) and the intrinsic tensile strength (S_0).

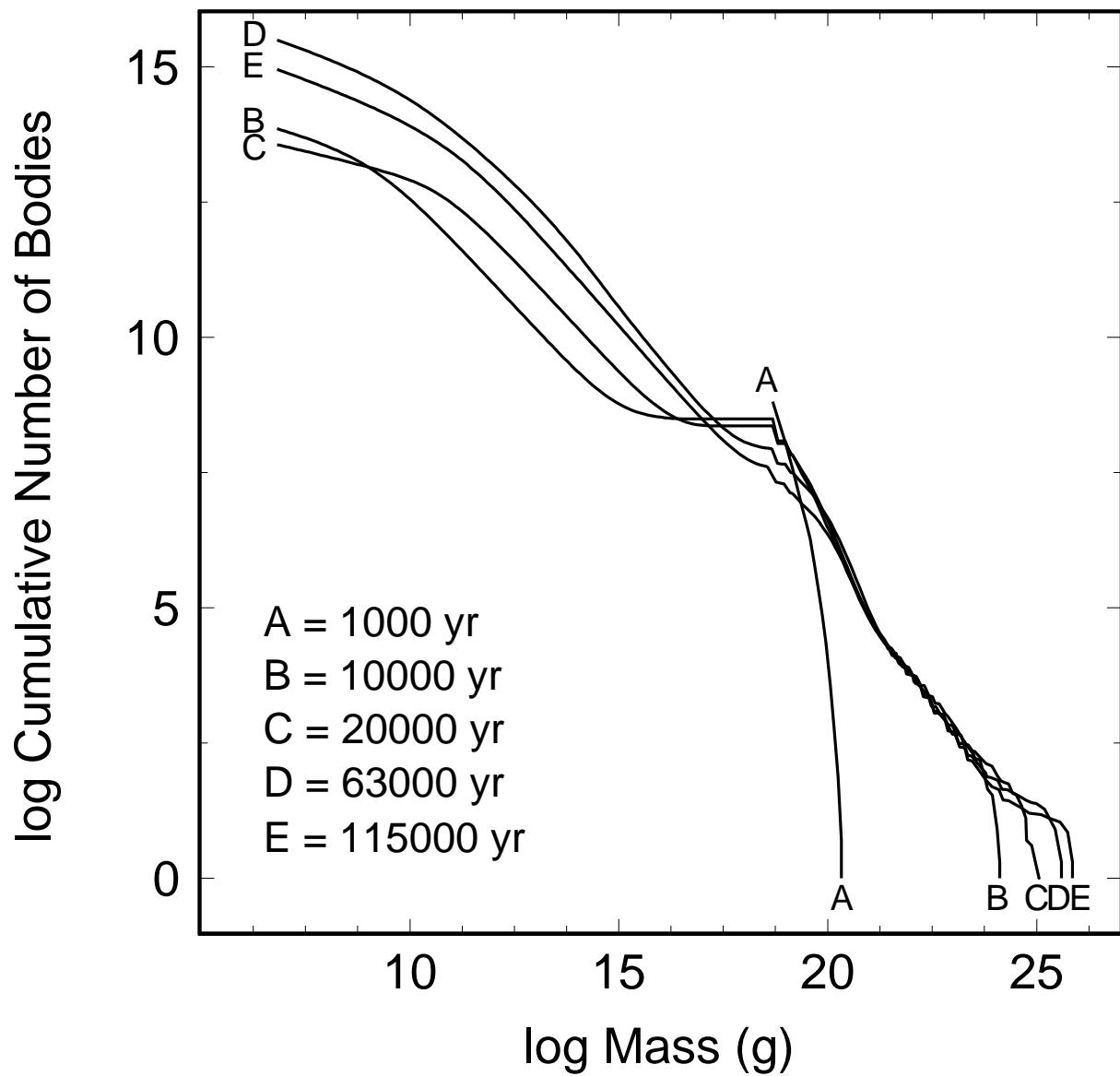


Fig. 1.— Cumulative mass distribution at selected times for a calculation at 1 AU with $M_0 = 0.667 M_E$ and $\delta = 1.25$. A group of runaway bodies with $m_i \gtrsim 10^{24}$ g forms at $\sim 10^4$ yr. These batches contain 13% of the initial mass at 6.3×10^4 yr and 17% at 1.15×10^5 yr.

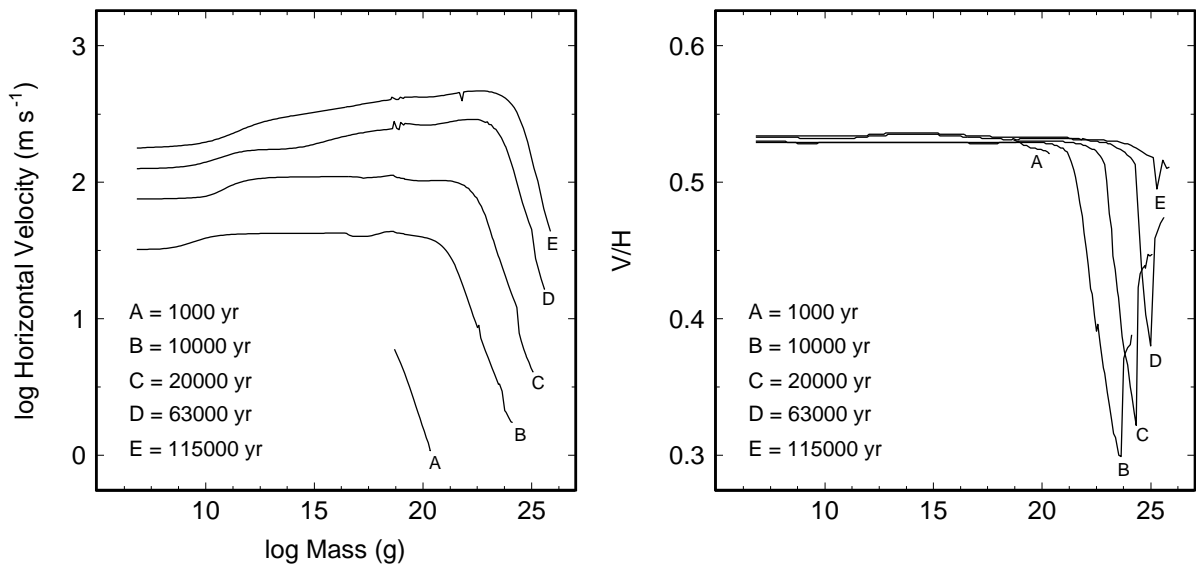


Fig. 2.— Velocity evolution for the 1 AU model in Fig. 1. (a) Horizontal velocity distribution. Viscous stirring increases all velocities with time; dynamical friction brakes the runaway bodies and increases velocities of the lowest mass bodies. (b) Ratio of vertical to horizontal velocity. The ratio remains close to the equilibrium value of $V/H = 0.53$ for all but the most massive objects, where $V/H \sim 0.3-0.5$.

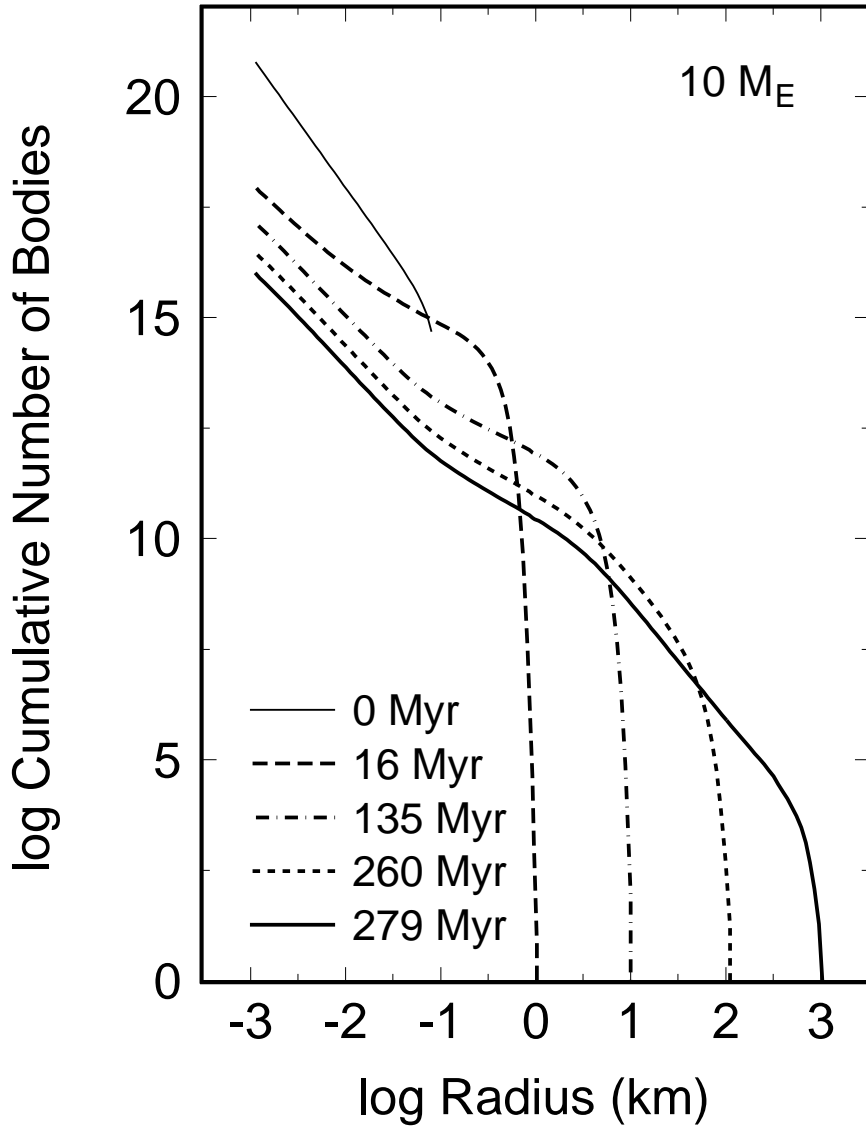


Fig. 3.— Cumulative size distributions for a Kuiper Belt model with $M_0 = 10 M_E$ and $c_1 = c_2 = 10^{-5}$. The eccentricity is constant in time at $e = 10^{-3}$. Collisional growth is slow for 200 Myr until the largest bodies have $r_{max} = 50$ km. Runaway growth begins when $r_{max} \gtrsim 100$ km. These bodies then grow to sizes of 10^3 km to 10^4 km in 20–30 Myr. The size distribution consists of a fragmentation tail with $N_c \propto r_i^{-2.25}$ for $r_i \lesssim 0.1$ km, a transition region with a flatter size distribution, and an accretion component with $N_C \propto r_i^{-2.6}$.

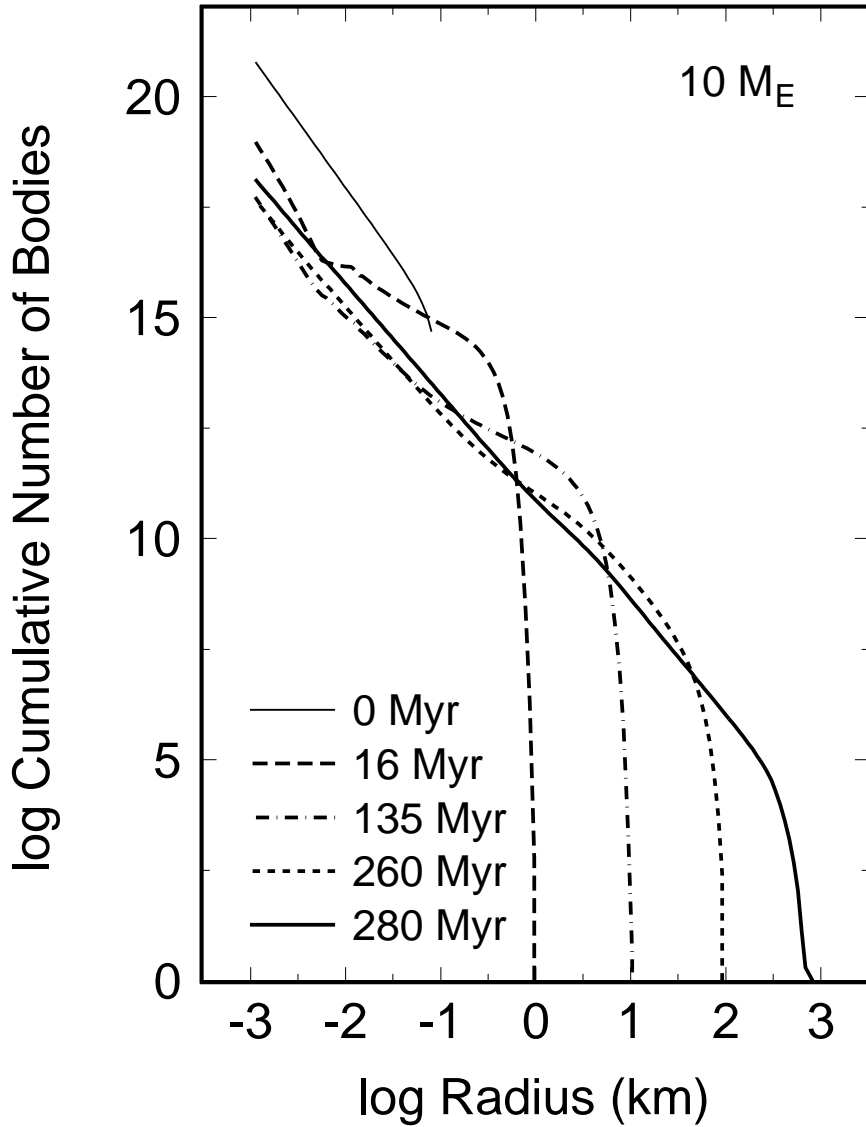


Fig. 4.— Cumulative size distributions for a Kuiper belt model with $M_0 = 10 M_E$, $c_1 = 10^{-2}$, and $c_2 = 10^{-3}$. The eccentricity is constant in time at $e_0 = 10^{-3}$. The evolution is identical to that in Figure 3, except for the appearance of a ‘kink’ in the size distribution due to rebounds at $r_i \approx 5$ m. As the evolution proceeds, debris from collisions with $r_i \gg 5$ m suppresses this kink and the size distribution more closely follows the $N_c \propto r_i^{-2.5}$ derived in calculations without rebounds.

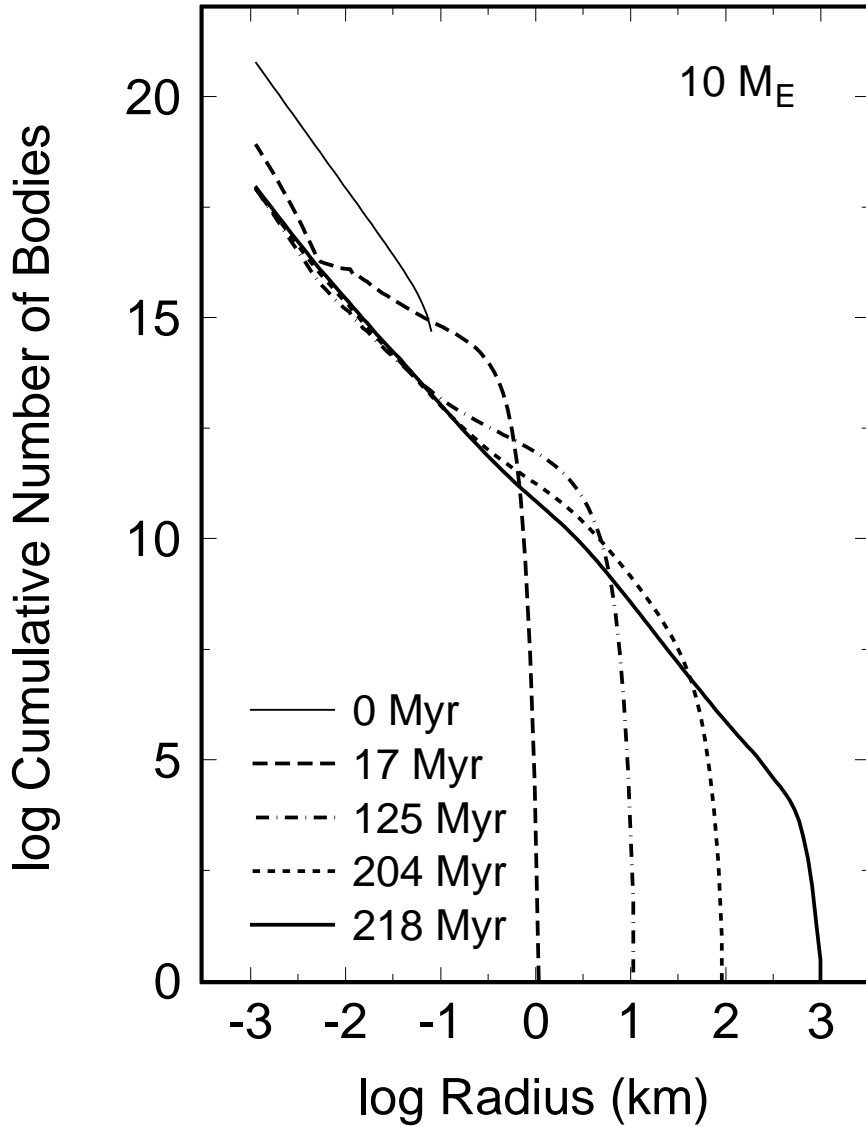


Fig. 5.— Cumulative size distributions for a Kuiper belt model with $M_0 = 10 M_E$, $c_1 = 10^{-2}$, $c_2 = 10^{-3}$, and limited velocity evolution. Eccentricity changes are due to fragmentation, which places a fixed fraction f_{KE} of the kinetic energy of each collision into the debris. The size distribution develops a kink at $r_i \approx 5$ m due to rebounds at 10–50 Myr when $r_{max} \approx 1$ –3 km. As the maximum radius increases, the size distribution approaches a smooth power law distribution, $N_C \propto r_i^{-2.5}$ from $r_i = 1$ m up to $r_i = 300$ –500 km.

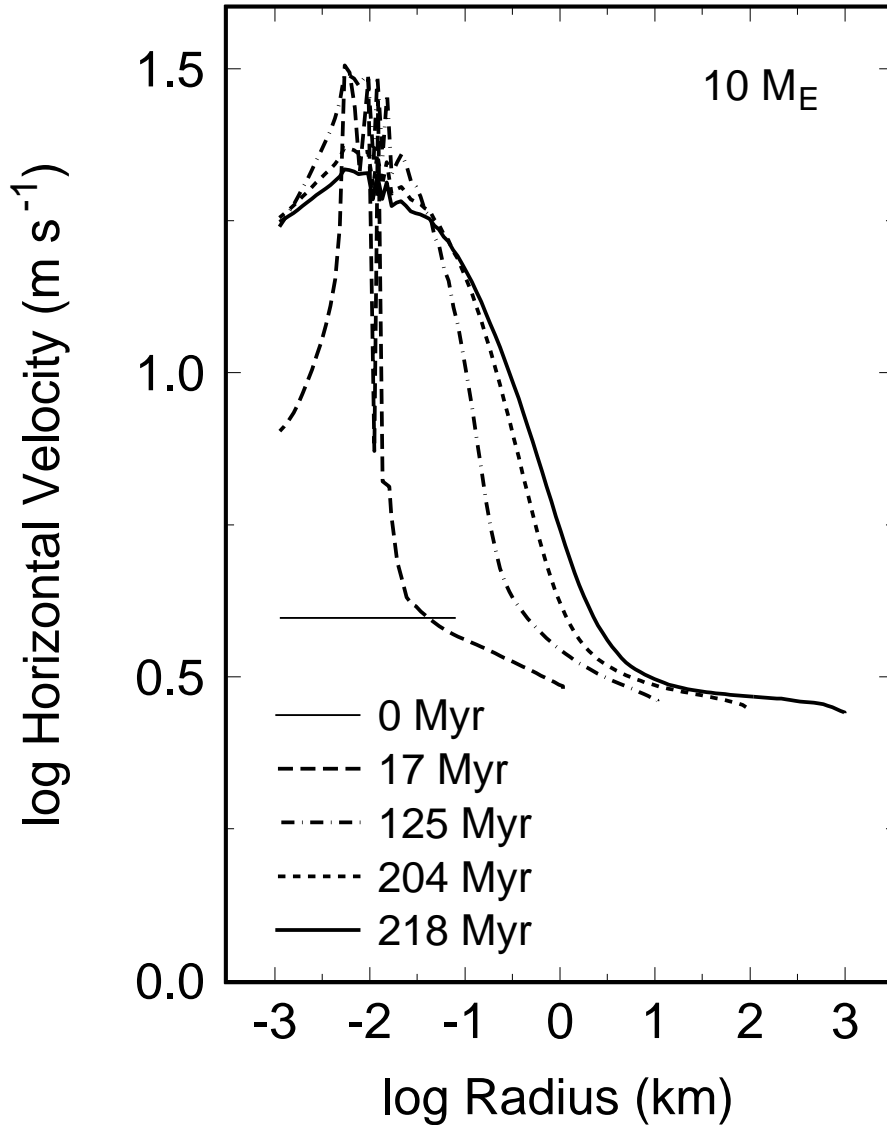


Fig. 6.— Horizontal velocity distributions as a function of time for the limited velocity evolution model in Figure 5. The velocity dispersion of all bodies begins at $h_i = 4 \text{ m s}^{-1}$. As the maximum radius increases from $r_{max} = 80 \text{ m}$ to $r_{max} = 1 \text{ km}$, collision debris increases the velocity of low mass bodies. This increase is most pronounced for bodies with $r_i \sim 10 \text{ m}$ at early times, because rebounds reduce the velocities of the lowest mass objects (dotted line). The high velocity dispersion propagates to bodies with $r_i = 1\text{--}100 \text{ m}$ as rebounds become less frequent and as mergers of the largest bodies produce more debris (dot-dashed and dashed lines). Once $r_{max} \approx 1000 \text{ km}$, the velocity distribution has settled into a high velocity component at $r_i \sim 1\text{--}100 \text{ m}$, a transition component at $r_i \sim 0.1\text{--}3 \text{ km}$, and a group of large objects, $r_i \gtrsim 3\text{--}5 \text{ km}$ with $h_i \approx 3 \text{ m s}^{-1}$.

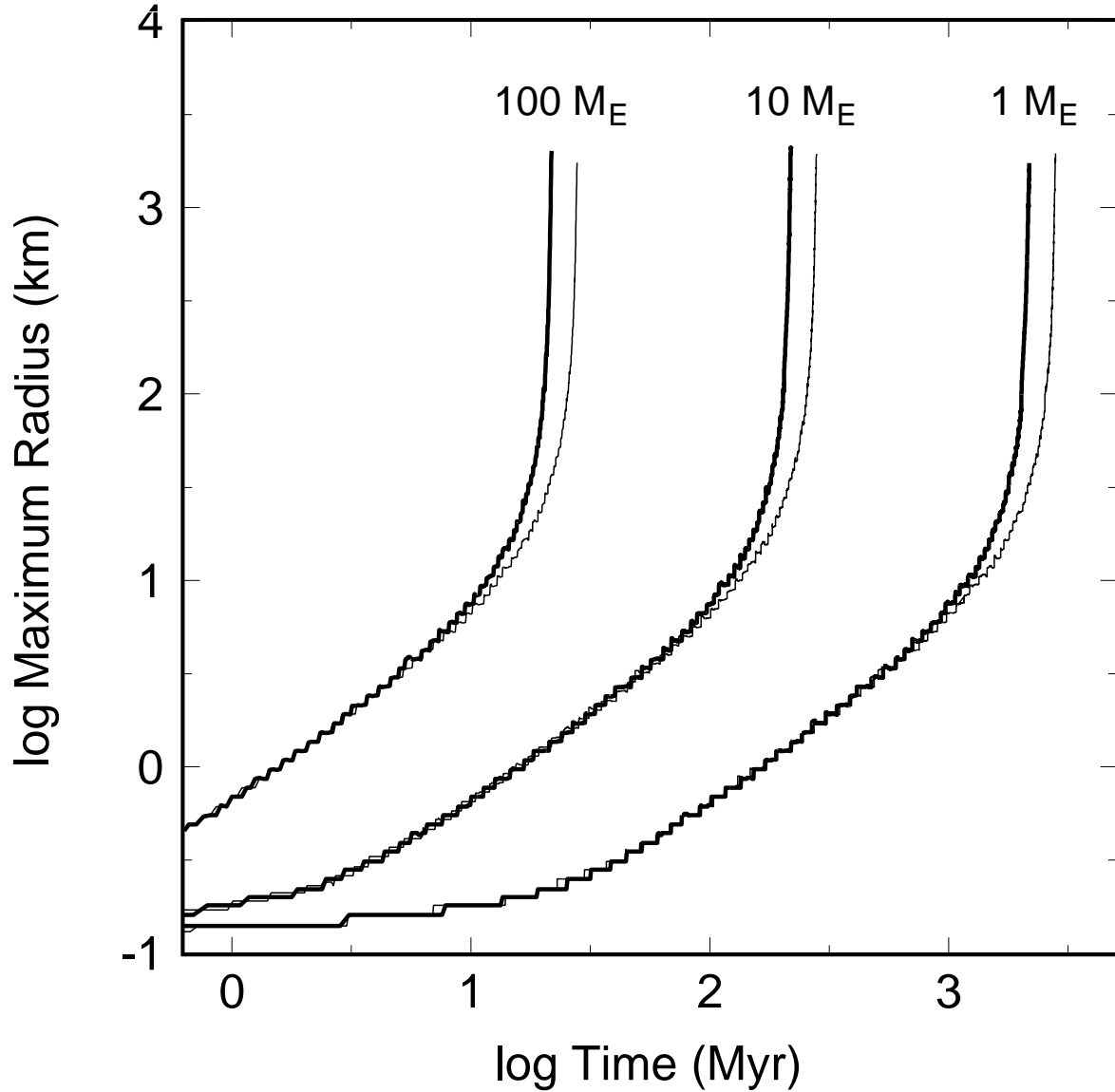


Fig. 7.— Maximum radius as a function of initial mass for models with no velocity evolution (thin solid lines) and limited velocity evolution (thick solid lines). The initial eccentricity is $e_0 = 10^{-3}$. The time to produce 1000 km objects scales inversely with initial mass, $\tau_P \approx \tau_0 (M_0/10M_E)^{-1}$, with $\tau_0 \approx 276\text{--}280$ Myr for models with no velocity evolution and $\tau_0 \approx 216$ Myr for models with limited velocity evolution. Fragmentation speeds up the growth of models with limited velocity evolution by redistributing kinetic energy from large objects to small objects.

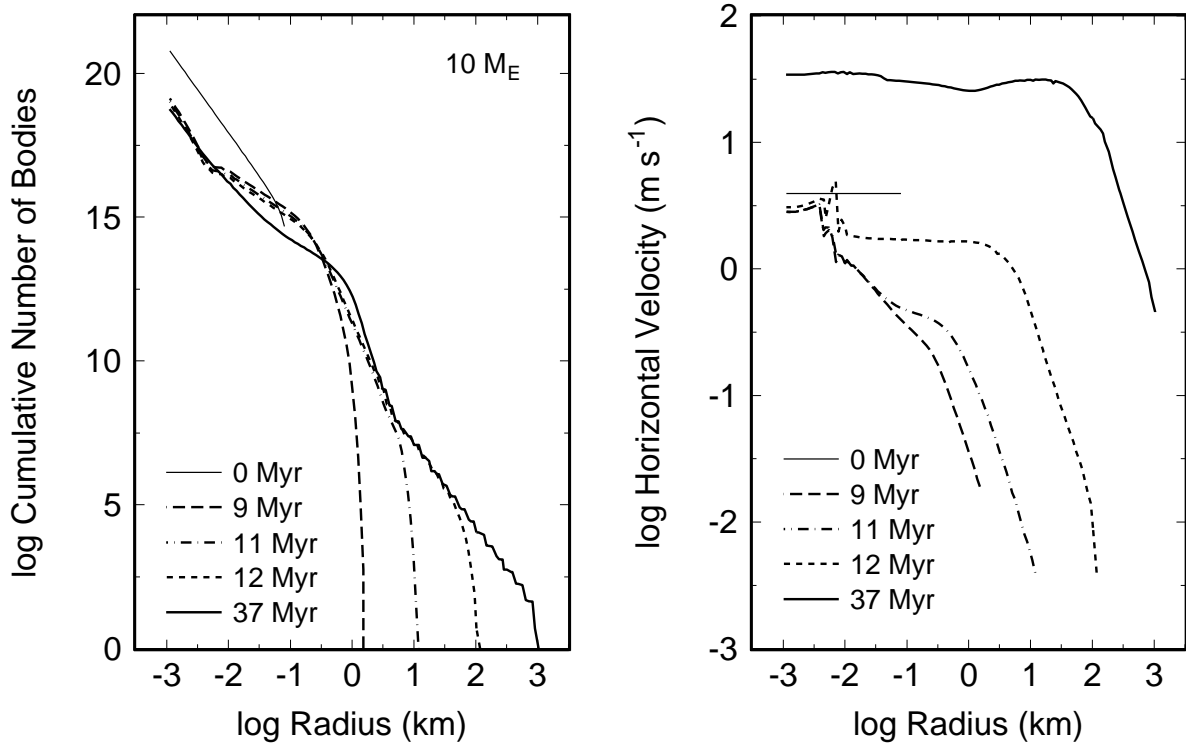


Fig. 8.— Size and velocity distributions for a model with $M_0 = 10 M_E$, $e_0 = 10^{-3}$, $S_0 = 2 \times 10^6 \text{ erg g}^{-1}$, and velocity evolution: (a) cumulative size distribution, and (b) horizontal velocity as a function of time. Collisional growth is slow until the largest bodies have $r_{max} = 1\text{--}2 \text{ km}$ at 9–10 Myr. Collisional damping reduces the velocities of all bodies to $\sim 1\text{--}2 \text{ m s}^{-1}$ on this timescale; dynamical friction reduces the velocities of larger bodies to $\sim 10^{-2} \text{ m s}^{-1}$. Runaway growth then produces objects with radii of 100 km in another 2–3 Myr. Viscous stirring increases particle velocities as objects grow to sizes of 100–300 km, and runaway growth ends. A prolonged linear growth phase leads to the production of 1000 km objects; the horizontal velocities are then $\sim 30\text{--}40 \text{ m s}^{-1}$ for the smallest objects and $\sim 1 \text{ m s}^{-1}$ for the largest objects.

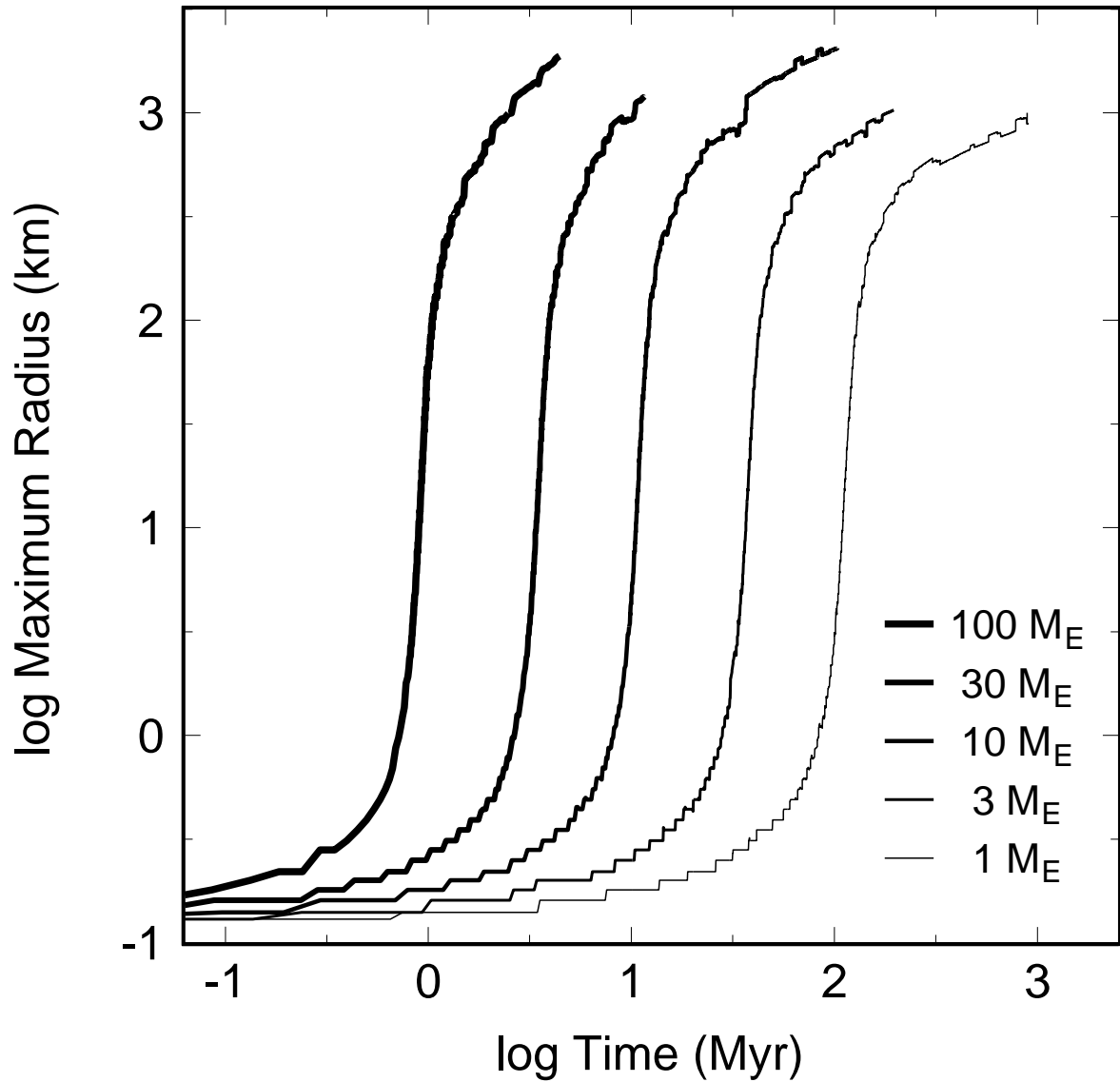


Fig. 9.— Evolution of the maximum radius, r_{max} , with time as a function of initial mass, M_0 , for $e_0 = 10^{-3}$. The timescale to reach runaway growth decreases with increasing M_0 .

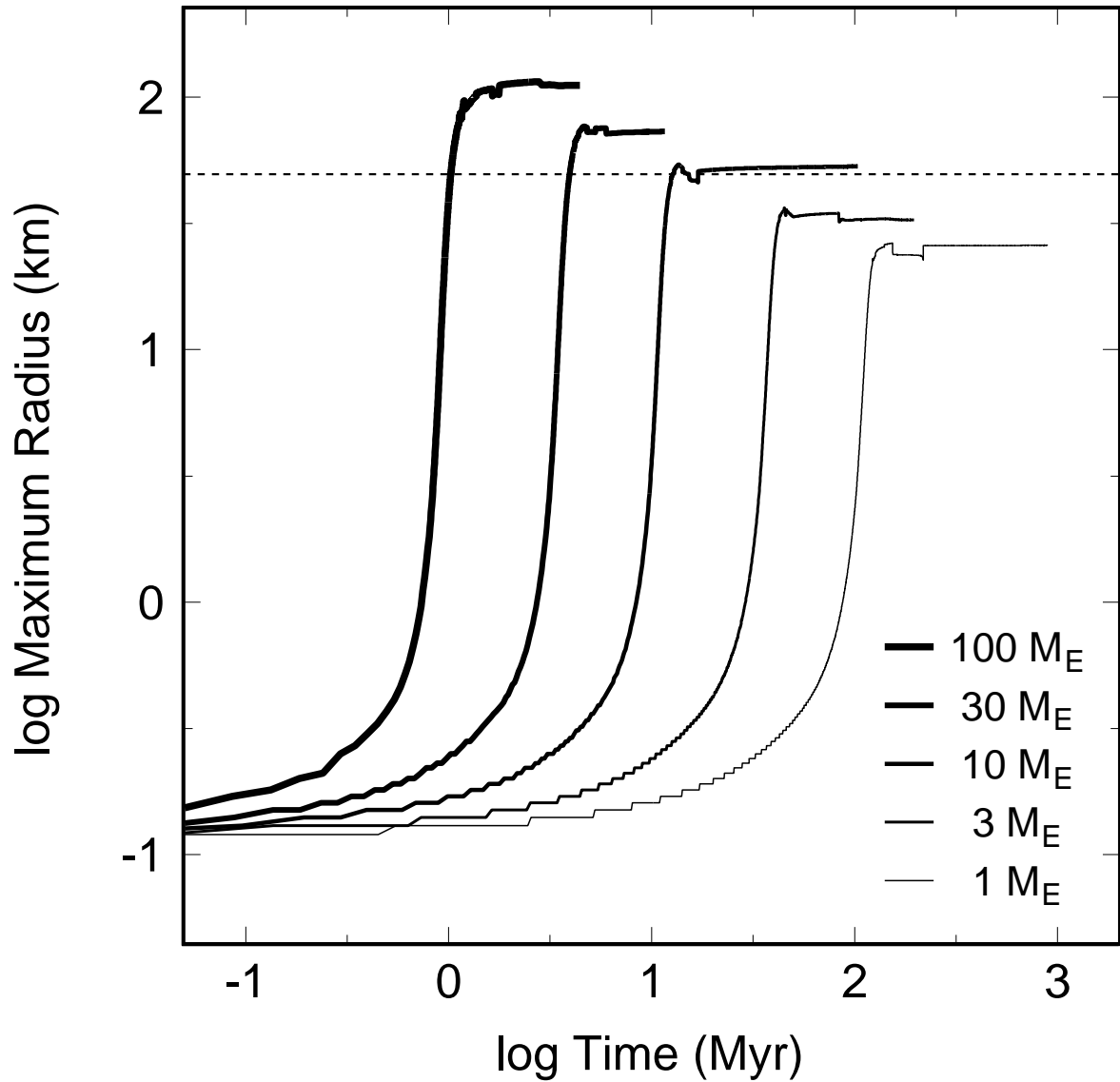


Fig. 10.— Evolution of r_5 , the radius where the cumulative number of objects is 10^5 , with time as a function of initial mass, M_0 , for $e_0 = 10^{-3}$. The constraint on r_5 set by current observations is indicated by the horizontal dashed line.

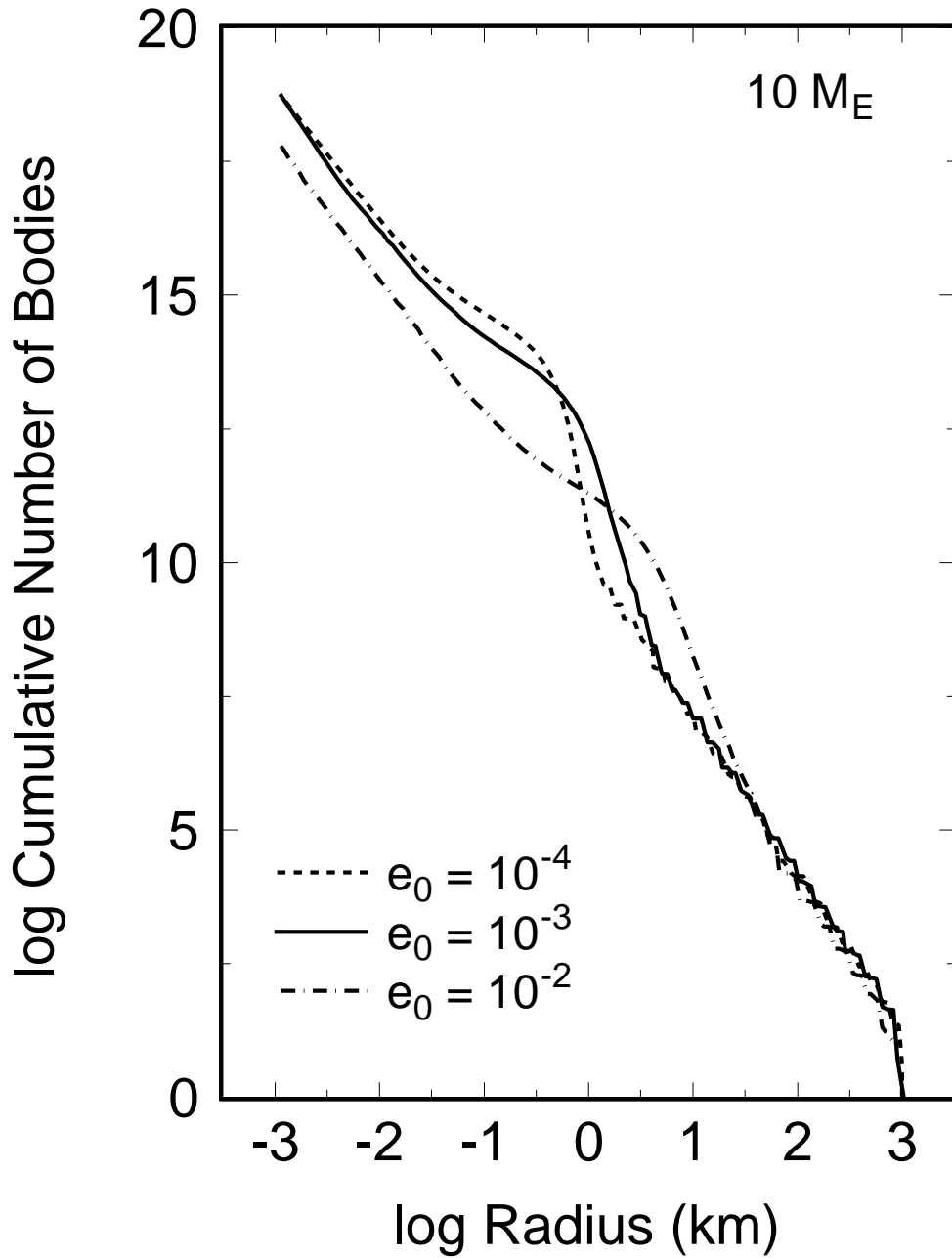


Fig. 11.— Cumulative size distribution when $r_{max} = 1000$ km for three values of the initial eccentricity, e_0 . Each size distribution follows two power laws, $N_C \propto r^{-2.5}$ at small radii and $N_C \propto r^{-3}$ at large radii. The transition between the two power laws moves to larger radii as e_0 increases.

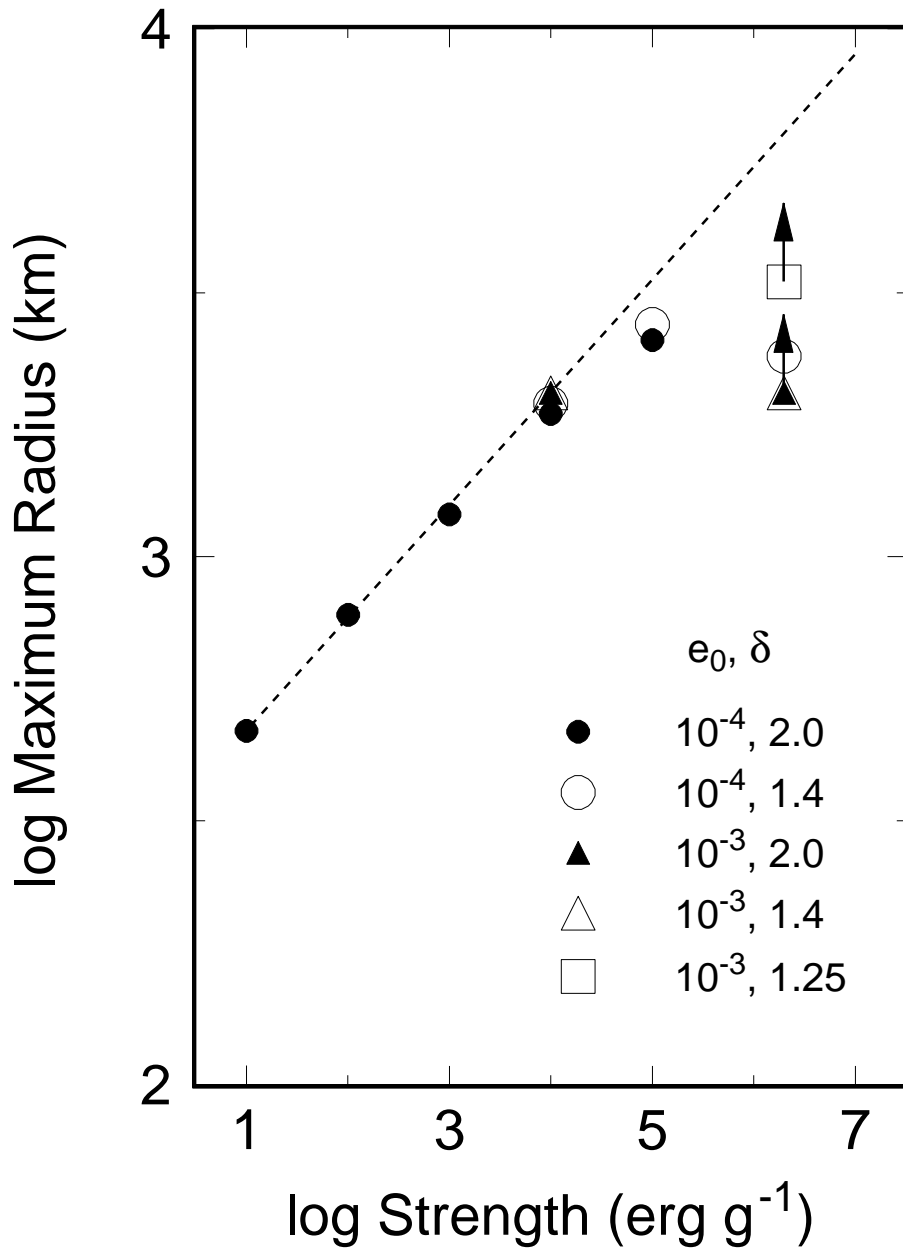


Fig. 12.— Maximum radius as a function of strength for models with $M_0 = 10 M_E$ and various e_0 and δ as listed in the legend.

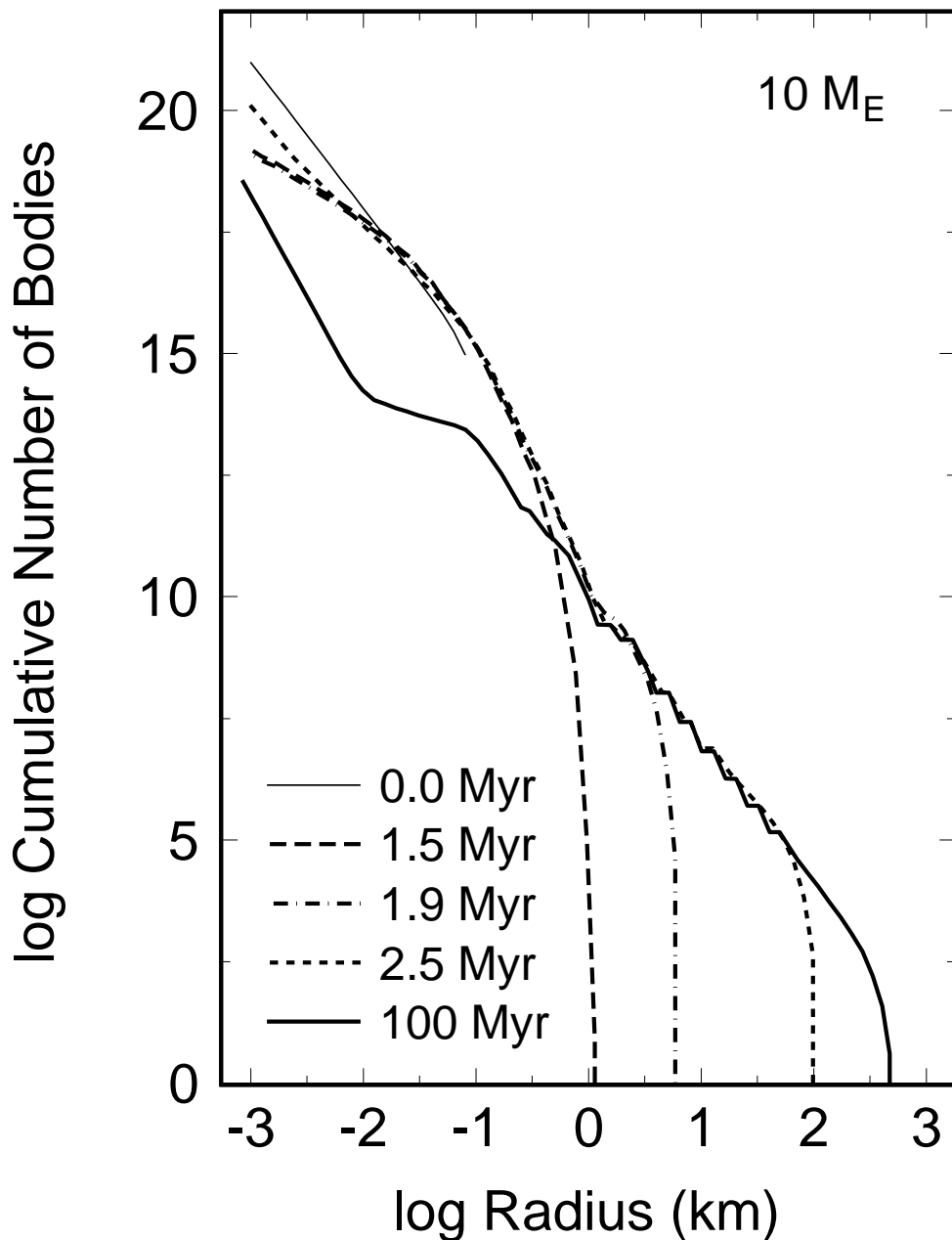


Fig. 13.— Cumulative size distributions for a model with $M_0 = 10 M_E$, $e_0 = 10^{-4}$, and $S_0 = 100 \text{ erg g}^{-1}$. Runaway growth produces objects with $r_{max} \approx 100 \text{ km}$ as in the standard model with $S_0 = 3 \times 10^6 \text{ erg g}^{-1}$. Catastrophic disruption begins when $r_{max} \approx 400 \text{ km}$. Continued mass loss due to catastrophic disruption reduces the population of low mass objects with $r_i \lesssim 0.1 \text{ km}$, which are completely removed from the distribution for $\tau \gtrsim 100 \text{ Myr}$.